

# Towards Generalisable Time Series Understanding Across Domains

Özgün Turgut<sup>1,2</sup> Philip Müller<sup>1,2</sup> Martin J Menten<sup>1,3,4</sup> Daniel Rueckert<sup>1,2,3,4</sup>

## Abstract

Recent breakthroughs in natural language processing and computer vision, driven by efficient pre-training on large datasets, have enabled foundation models to excel on a wide range of tasks. However, this potential has not yet been fully realised in time series analysis, as existing methods fail to address the heterogeneity in large time series corpora. Prevalent in domains ranging from medicine to finance, time series vary substantially in characteristics such as variate count, inter-variate relationships, temporal patterns, and sampling frequency. To address this, we introduce a novel pre-training paradigm specifically designed to handle time series heterogeneity. We propose a tokeniser with learnable domain signatures, a dual masking strategy, and a normalised cross-correlation loss, enabling our open model for general time series analysis (OTiS) to efficiently learn from large time series corpora. Extensive benchmarking on diverse tasks, such as classification, regression, and forecasting, demonstrates that OTiS outperforms state-of-the-art baselines. Our code and pre-trained weights are available at <https://github.com/oetu/otis>.

## 1. Introduction

In natural language processing (NLP) or computer vision (CV), generalisable language features, e.g. semantics and grammar (Radford et al., 2018; Touvron et al., 2023; Chowdhery et al., 2023), or visual features, e.g. edges and shapes (Geirhos et al., 2019; Dosovitskiy et al., 2021; Oquab et al., 2024), are learned from large-scale data. Self-supervised pre-training paradigms are designed to account for the specific properties of language (Radford et al., 2018; Touvron et al., 2023; Chowdhery et al., 2023) or imaging (Zhou et al.,

<sup>1</sup>School of Computation, Information and Technology, Technical University of Munich, Germany <sup>2</sup>School of Medicine, Klinikum rechts der Isar, Technical University of Munich, Germany <sup>3</sup>Munich Center for Machine Learning, Munich, Germany <sup>4</sup>Department of Computing, Imperial College London, United Kingdom. Correspondence to: Özgün Turgut <oezguen.turgut@tum.de>.

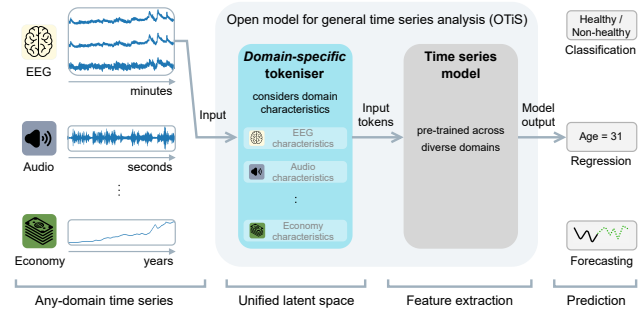


Figure 1. Open model for general time series analysis (OTiS). Its tokeniser accounts for varying time series characteristics across domains, such as distinct variate counts, inter-variate relationships, temporal patterns, and sampling frequencies. It can be fine-tuned on limited data from any domain, including previously unseen ones, to perform classification, regression, and forecasting tasks.

2022; Cherti et al., 2023; Oquab et al., 2024), unlocking foundational model capabilities that apply to a wide range of tasks. This potential, however, remains largely unrealised in time series due to the lack of pre-training paradigms that effectively address time series heterogeneity across domains.

Time series are widespread in everyday applications and play an important role in various domains, including medicine (Pirkis et al., 2021), engineering (Gasparin et al., 2022), natural sciences (Ravuri et al., 2021), and finance (Sezer et al., 2020). They differ substantially with respect to the number of variates, inter-variate relationships, temporal patterns, and sampling frequency (Fawaz et al., 2018; Ismail Fawaz et al., 2019; Ye & Dai, 2021; Wickstrøm et al., 2022). For instance, standard 10-20 system electroencephalography (EEG) recordings come with up to 256 variates (Jurcak et al., 2007), while most audio recordings have only 1 (mono) or 2 (stereo) variates. Weather data shows high periodicity, whereas financial data is exposed to long-term trends. Both domains encompass low-frequency data recorded on an hourly (278  $\mu$ Hz), daily (12  $\mu$ Hz), or even monthly (386 nHz) basis, while audio data is sampled at high frequencies of 44.1 kHz or more. Overall, this heterogeneity across domains renders the extraction of generalisable time series features difficult (Fawaz et al., 2018; Gupta et al., 2020; Iwana & Uchida, 2021; Ye & Dai, 2021).

While most existing self-supervised pre-training methods

for time series are limited to single domains (Wu et al., 2021; 2022a; Nie et al., 2023; Dong et al., 2024; Jiang et al., 2024), recent works propose simple techniques to incorporate time series from multiple domains (Yang et al., 2024; Das et al., 2024; Woo et al., 2024; Liu et al., 2024). These works, for instance, crop all time series into segments of unified size (Jiang et al., 2024), resample them to a uniform frequency (Yang et al., 2024), or analyse each variate of a multi-variate time series independently (Liu et al., 2024). While these naive techniques address domain differences in sampling frequency and variate count, they degrade the original time series and fail to account for inter-variate relationships and temporal patterns, which vary heavily across domains.

Consequently, there is a clear need for pre-training strategies that effectively address data heterogeneity across domains. In this work, we propose a novel multi-domain pre-training paradigm that accounts for the varying characteristics across domains. This approach enables our open model for general time series analysis (OTiS) to be pre-trained on a large and diverse time series corpus, unlocking foundational capabilities. Our key contributions can be summarised as follows:

1. We propose a novel multi-domain pre-training paradigm that enables the learning of generalisable time series features. We introduce a novel tokeniser to account for the varying characteristics across domains, a dual masking strategy to capture bidirectional relationships and temporal causality, and a normalised cross-correlation loss to learn global temporal patterns.
2. We pre-train OTiS on a large corpus spanning 8 domains from medicine, engineering, natural sciences, and finance. With 640, 187 samples and 11 billion time points, it covers diverse time series characteristics, essential for developing foundational model capabilities.
3. Evaluated across 15 applications, OTiS is competitive with specialised and general state-of-the-art models, setting new benchmarks in 10 tasks. Notably, none of the baselines can handle the variety of tasks covered by OTiS, i.e. classification, regression, and forecasting.

## 2. Related Works

### 2.1. Self-Supervised Learning for Time Series

Time series vary significantly across domains, with differences in the number of variates, inter-variate relationships, temporal patterns, and sampling frequencies. Due to this inherent heterogeneity, most existing works focus on pre-training models within a single domain (Oreshkin et al., 2019; Tang et al., 2020; Wu et al., 2021; Zhou et al., 2021; Wu et al., 2022a; Woo et al., 2022; Yue et al., 2022; Zhang et al., 2022; Li et al., 2023; Nie et al., 2023; Zeng et al., 2023; Dong et al., 2024). To develop more general time

series models, recent works have explored multi-domain pre-training by partially addressing this heterogeneity, including the different numbers of variates and sampling frequencies. Liu et al. (2024) treat each variate in a multi-variate time series independently to standardise generative tasks like forecasting, while Goswami et al. (2024) extend uni-variate analysis to discriminative tasks like classification. Jiang et al. (2024) and Yang et al. (2024) standardise time series by cropping them into segments of predefined size and resampling them to a uniform frequency, respectively, to enable general classification capabilities in medical domains.

While partially addressing time series heterogeneity, these pre-training paradigms cannot unlock foundational model capabilities. Standardisation techniques like cropping or resampling may distort inter-variate relationships and temporal patterns. Additionally, many of these approaches are tailored to specific applications, such as generative tasks (Das et al., 2024; Liu et al., 2024; Woo et al., 2024), or focus on domains in a particular field, like medicine (Jiang et al., 2024; Yang et al., 2024). Moreover, recent foundation models (Das et al., 2024; Goswami et al., 2024; Liu et al., 2024) focus on uni-variate analysis, ignoring inter-variate relationships that are essential for real-world applications, such as disease prediction (Schoffelen & Gross, 2009; Wu et al., 2022b). Our study aims to overcome these limitations by effectively addressing time series heterogeneity, establishing a robust foundation for general time series analysis.

### 2.2. Time Series Tokenisation

Transformers (Vaswani et al., 2017) have emerged as the preferred architecture for foundation models in NLP and CV due to their scalability (Kaplan et al., 2020; Gordon et al., 2021; Alabdulmohsin et al., 2022), enabling the training of large models (Chowdhery et al., 2023; Touvron et al., 2023; Oquab et al., 2024; Ravi et al., 2024). To utilise a Transformer for time series analysis, a tokeniser is required to map the time series into a compact latent space. Current methods (Jin et al., 2023; Nie et al., 2023; Zhou et al., 2023; Das et al., 2024; Goswami et al., 2024; Jiang et al., 2024; Liu et al., 2024; Woo et al., 2024; Yang et al., 2024) follow established techniques from NLP and CV, dividing time series into patches of pre-defined size. These patches are then flattened into a 1D sequence, with positional embeddings used to retain positional information. While uni-variate models (Nie et al., 2023; Das et al., 2024; Goswami et al., 2024; Liu et al., 2024) consider only temporal positions, multi-variate approaches (Woo et al., 2024; Yang et al., 2024; Jiang et al., 2024) account for both temporal and variate positions. However, none of the current methods consider the varying characteristics across domains, e.g. mistakenly assuming that the relationships between variates are identical across domains. Our work seeks to adapt time series tokenisation to account for these domain-specific characteristics.

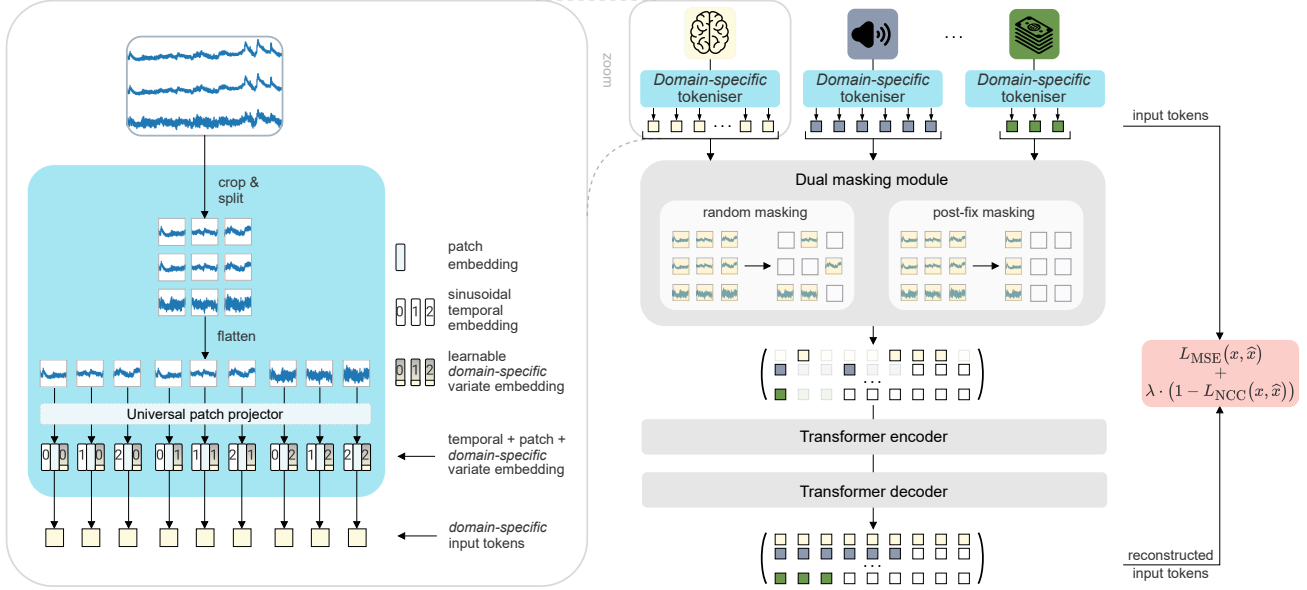


Figure 2. Pre-training of OTiS. A time series is split into fixed-size patches, which are then embedded using a universal patch projector. In addition to a temporal embedding, each patch embedding is modulated with a *domain-specific* variate embedding to account for the unique characteristics of a domain. The resulting input tokens are masked with a dual masking strategy and reconstructed to optimise OTiS. The reconstruction is guided by a combination of mean squared error (MSE) and normalised cross-correlation (NCC) loss terms.

### 3. Methods

In this work, we present a novel multi-domain pre-training paradigm that enables the extraction of generalisable time series features. We introduce a tokeniser that accounts for varying time series characteristics across domains (see Section 3.1). We tailor masked data modelling to multi-domain time series, enabling our **open** model for general **time** series analysis (OTiS) to be pre-trained on a large, heterogeneous corpus (see Section 3.2). In particular, we introduce normalised cross-correlation as a loss term to capture global temporal patterns in time series (see Section 3.3) and propose a dual masking strategy to model both bidirectional relationships and temporal causality in time series (see Section 3.4). After pre-training, OTiS can be fine-tuned on limited data from any domain, including previously unseen ones, to perform general time series tasks, such as classification, regression, and forecasting (see Section 3.5).

#### 3.1. Domain-Specific Tokeniser

**Overview.** Assume a time series sample  $\mathbf{X} \in \mathbb{R}^{V_S \times T}$  from domain  $S$ , where  $V_S$  denotes the number of variates specific to  $S$  and  $T$  denotes the number of time points. We randomly crop or zero-pad  $\mathbf{X}$  to a fixed context length of  $\bar{T}$  time points. We then split it into  $T'$  temporal patches of size  $P$  along the time dimension, resulting in  $V_S \cdot T'$  patches  $x_{v,t} \in \mathbb{R}^{1 \times P}$ , where  $v \in \{1, \dots, V_S\}$  and  $t \in \{1, \dots, T'\}$ .

Next, we embed these patches using a universal patch pro-

jector shared across domains, producing patch embeddings  $e^P(x_{v,t}) = e_{v,t}^P \in \mathbb{R}^{1 \times D}$ , where  $D$  denotes the model dimension. The patch projector consists of a 1D convolutional layer followed by layer normalisation and GELU activation. With a unified patch size and a domain-agnostic design, it serves as a general feature extractor and is inherently *frequency-agnostic*. While the sampling frequency varies across domains, it consistently ensures that relevant information is captured within the observation period, i.e. time series. Hence, as long as a model’s context length is sufficiently long, it has access to the relevant information within a time series, regardless of the sampling frequency.

The permutation-equivariant nature of Transformers (Vaswani et al., 2017) requires the use of positional embeddings to accurately capture the inherent relationships of the input. Initially introduced for 1D textual sequences (Vaswani et al., 2017), positional embeddings simply introduce an ordering into the input sequence. Modern implementations extend their capabilities to encode more complex geometric information, such as 2D spatial (Dosovitskiy et al., 2021) or graph (Kreuzer et al., 2021) structures. In this work, we differentiate between temporal and variate structures for the analysis of any-variate time series. The temporal structure is equivalent to a 1D sequence, such that we use standard 1D sinusoidal embeddings  $e^T(x_{v,t}) = e_t^T \in \mathbb{R}^{1 \times D}$ .

The variate structure exhibits great heterogeneity across domains. In domains with uni-variate and two-variate data, such as mono and stereo audio, the structure is either trivial

or only requires a basic distinction between variates. In other domains, however, the variate structure may represent more complex relationships, such as 3D manifolds for electroencephalography (EEG) or electrocardiography (ECG), or be of non-spatial nature, e.g. for financial data. To account for these varying characteristics across domains, we introduce learnable *domain-specific* variate embeddings. These embeddings, denoted as  $e_S^V(x_{v,t}) = e_{S,v}^V \in \mathbb{R}^{1 \times D}$  for each variate  $v$  in domain  $S$ , are designed to capture the unique characteristics of a domain  $S$ , including the domain-specific inter-variate relationships and temporal patterns. Hence, they can be considered as a *domain signature* after training.

Finally, the patch, temporal, and domain-specific variate embeddings are summed to form the input token  $e_{v,t} = e_{v,t}^P + e_t^T + e_{S,v}^V \in \mathbb{R}^{1 \times D}$ . These tokens collectively form the final input sequence  $\mathbf{E} \in \mathbb{R}^{(V_S \cdot T') \times D}$ . As time series across domains vary in the number of variates, we pad the variate dimension to the maximum number of variates  $\bar{V} = \max_S V_S$  within each batch. For samples where  $V_S < \bar{V}$  or  $T < \bar{T}$ , attention masking is used to ensure that padded variate or temporal tokens are ignored. The domain-specific tokeniser is trained end-to-end with the Transformer layers.

**Definition of Domains.** The domain-specific tokeniser is designed to integrate different datasets within a domain. Consider two EEG datasets, TDBrain (Van Dijk et al., 2022) and SEED (Zheng & Lu, 2015), which share 19 identical variates but have different sampling frequencies of 500 Hz and 200 Hz, respectively. In this case, a single EEG-specific tokeniser ( $V_{\text{EEG}} = 19$ ) is sufficient to accommodate both sampling frequencies, i.e.  $\mathbf{E}_{\text{EEG-TDBrain}}^V = \mathbf{E}_{\text{EEG-SEED}}^V = [e_{\text{EEG},1}^V, \dots, e_{\text{EEG},19}^V]^\top \in \mathbb{R}^{19 \times D}$ , as shown in our experiments in Section 4. Note that while these positional embeddings are agnostic to variate ordering, we simplify processing by aligning the variate order across datasets within a domain. Consider another EEG dataset, LEMON (Babayan et al., 2019), with 62 variates. Of these, 15 overlap with the variates in TDBrain (Van Dijk et al., 2022) and SEED (Zheng & Lu, 2015), while the remaining 47 are unique to LEMON (Babayan et al., 2019). In this scenario, the EEG-specific tokeniser can be extended by the 47 new variates ( $V_{\text{EEG}} = 66$ ), such that  $\mathbf{E}_{\text{EEG-LEMON}}^V = [e_{\text{EEG},1}^V, \dots, e_{\text{EEG},15}^V, e_{\text{EEG},20}^V, \dots, e_{\text{EEG},66}^V]^\top \in \mathbb{R}^{66 \times D}$ . In this way, different datasets can be combined to approximate the underlying data distribution of a domain, e.g. EEG, enabling the creation of large and diverse time series corpora.

**Multi-Variate or Uni-Variate Analysis?** Consider the Electricity dataset (UCI, 2024), which contains electricity consumption data for 321 households recorded from 2012 to 2014. These 321 observations are sampled from an underlying population and are assumed to be independent and identically distributed (*i.i.d.*). In this scenario, we perform a

uni-variate analysis ( $V_{\text{Electricity}} = 1$ ) of the data, initialising a single Electricity-specific variate embedding that models the hourly consumption of a household. In contrast, the Weather dataset (Wetterstation, 2024) contains 21 climatological indicators, such as air temperature, precipitation, and wind speed, which are not *i.i.d.* because they directly interact and correlate with one another. Therefore, a multi-variate analysis ( $V_{\text{Weather}} = 21$ ) is conducted to account for the dependencies and interactions between the observations.

### 3.2. Pre-Training on Multi-Domain Time Series

To learn generalisable time series features, we adapt masked data modelling (MDM) (He et al., 2022) and pre-train OTIS on multi-domain time series, as visualised in Figure 2. We mask a subset of the input tokens and only encode the visible tokens using an encoder  $f(\cdot)$ . We then complement the encoded tokens with learnable mask tokens and pass them through a decoder  $g(\cdot)$  to reconstruct the input tokens.

More precisely, we draw a binary mask  $m \in \{0, 1\}^{V_S \cdot T'}$ , following a dual masking strategy introduced in Section 3.4, and apply it to the input sequence  $\mathbf{E} \in \mathbb{R}^{(V_S \cdot T') \times D}$ . Thus, we obtain a visible view  $\mathbf{E}[m] \in \mathbb{R}^{N_1 \times D}$ , where  $N_1 = \sum_{v=1}^{V_S} \sum_{t=1}^{T'} m_{v,t}$  and  $N_0 = (V_S \cdot T') - N_1$  denote the number of visible and masked tokens, respectively. The visible tokens  $\mathbf{E}[m]$  are then fed to the encoder  $f(\cdot)$  to compute the time series features  $\mathbf{H} \in \mathbb{R}^{N_1 \times D}$ :

$$\mathbf{H} = f(\mathbf{E}[m]). \quad (1)$$

To reconstruct the original input tokens, these features are passed through the decoder  $g(\cdot)$  along with a learnable mask embedding  $e^{\mathcal{M}} \in \mathbb{R}^{1 \times D}$ , which is inserted at each masked position where  $m_{v,t} = 0$ :

$$h'_{v,t} = \begin{cases} h_{v,t} & \text{if } m_{v,t} = 1 \\ e^{\mathcal{M}} + e_t^T + e_{S,v}^V & \text{if } m_{v,t} = 0 \end{cases}, \quad (2)$$

such that  $\mathbf{H}' \in \mathbb{R}^{(V_S \cdot T') \times D}$ . The decoder  $g(\cdot)$  then predicts the reconstructed input  $\widehat{\mathbf{X}} \in \mathbb{R}^{V_S \times (T' \cdot P)}$ :

$$\widehat{\mathbf{X}} = g(\mathbf{H}'), \quad (3)$$

where  $(T' \cdot P) = \bar{T}$ , i.e. the context length specified in time points. Eventually, the domain-specific tokeniser described in Section 3.1, the encoder  $f(\cdot)$ , and the decoder  $g(\cdot)$  are optimised end-to-end using the mean squared error (MSE) loss on all reconstructed input tokens:

$$\mathcal{L}_{\text{MSE}} = \frac{1}{V_S \cdot T'} \sum_{v=1}^{V_S} \sum_{t=1}^{T'} \|x_{v,t} - \widehat{x}_{v,t}\|_2^2. \quad (4)$$

### 3.3. Normalised Cross-Correlation Loss

MDM focuses on reconstructing masked parts of the data, emphasising *local* patterns through the MSE loss (4). However, time series often exhibit long-range dependencies,

where past values influence future outcomes over extended periods. To accurately capture these *global* patterns, we introduce normalised cross-correlation (NCC) as a loss term

$$\mathcal{L}_{\text{NCC}} = \frac{1}{V_S \cdot \bar{T}} \sum_{v=1}^{V_S} \sum_{t=1}^{\bar{T}} \frac{1}{\sigma_{x_v} \sigma_{\hat{x}_v}} (x_{v,t} - \mu_{x_v})(\hat{x}_{v,t} - \mu_{\hat{x}_v}) \quad (5)$$

for MDM in time series, where  $\mu$  and  $\sigma$  denote the mean and standard deviation, respectively, and  $\mathcal{L}_{\text{NCC}} \in [-1, 1]$ . Hence, to capture both local and global temporal patterns, the total loss used to optimise OTiS is defined as

$$\mathcal{L} = \mathcal{L}_{\text{MSE}} + \lambda \cdot (1 - \mathcal{L}_{\text{NCC}}), \quad (6)$$

where  $\lambda \in \mathbb{R}$  is empirically set to 0.1 during pre-training.

### 3.4. Dual Masking Strategy

We design the masking strategy to enhance foundational model capabilities in time series analysis. Specifically, we randomly select between two masking schemes during pre-training, namely random masking and post-fix masking. In 75% of cases, we apply random masking, where each  $m_{v,t}$  is independently sampled from a Bernoulli distribution with probability  $p = 1 - \rho$ , with  $\rho \in [0, 1]$  denoting the masking ratio (i.e.  $m_{v,t} \sim \text{Bernoulli}(1 - \rho)$ ). This encourages the model to learn complex inter-variate relationships across the entire time series. In the remaining 25% of cases, we employ post-fix masking, which masks the second half of the temporal dimension, leaving only the first half visible (i.e.  $m_{v,t} = \mathbb{1}_{[t \leq T'/2]}$ ). The prediction of future values solely based on past observations simulates real-world forecasting conditions, helping the model to capture temporal causality. Note that the optimal balance between the two masking schemes is empirically determined (see Appendix G.1). Overall, this dual masking strategy enables OTiS to learn both bidirectional relationships and temporal causality, which prove essential for general time series analysis.

### 3.5. Fine-Tuning & Inference

**Adaptation to Unseen Domains.** For a previously unseen domain  $S$ , we randomly initialise variate embeddings  $\mathbf{E}_S^V \in \mathbb{R}^{V_S \times D}$ . These embeddings are then fine-tuned along with the pre-trained encoder  $f(\cdot)$  and, if required, the decoder  $g(\cdot)$ , for the specific task in  $S$ , as detailed in the following.

**Classification & Regression.** We use the pre-trained encoder  $f(\cdot)$  and the unmasked input sequence  $\mathbf{E}$  to extract the time series features  $\mathbf{H} = f(\mathbf{E}) \in \mathbb{R}^{(V_S \cdot T') \times D}$ . We average-pool these features into a global representation  $h^* \in \mathbb{R}^{1 \times D}$ , which is passed through a linear layer to obtain the final model prediction. We optimise a cross-entropy and MSE loss for the classification and regression tasks, respectively.

Table 1. Overview of our pre-training corpus that spans eight domains from medicine, engineering, natural sciences, and finance.

Domain	Name	Samples	Variates	Time points	Frequency
ECG	MIMIC-IV-ECG	400,000	12	5,000	500 Hz
Temperature	DWD	203,340	1	720	278 $\mu$ Hz
Audio (stereo)	AudioSet-20K	16,123	2	441,000	44.1 kHz
Audio (mono)	AudioSet-20K	3,491	1	441,000	44.1 kHz
Electromechanics	FD-A	13,640	1	5,120	64 kHz
EEG	TDBrain	2,692	19	60,000	500 Hz
EEG	SEED	675	19	37,000	200 Hz
Banking	NN5	111	1	971	12 $\mu$ Hz
Economics	FRED-MD	107	1	728	386 nHz
Economics	Exchange	8	1	7,588	12 $\mu$ Hz
		<b>640,187</b>		<b>11,052,756,981</b>	

**Forecasting.** We use the pre-trained encoder  $f(\cdot)$  and the unmasked input sequence  $\mathbf{E}$  to extract the time series features  $\mathbf{H} = f(\mathbf{E}) \in \mathbb{R}^{(V_S \cdot T') \times D}$ . We then concatenate the sequence with learnable mask embeddings  $e^{\mathcal{M}}$  to form  $\mathbf{H}' \in \mathbb{R}^{(V_S \cdot (T' + T'_H)) \times D}$ , where  $T'_H \cdot P$  denotes the forecasting horizon specified in time points. This input sequence is then passed through the pre-trained decoder  $g(\cdot)$  to obtain the final model prediction. We optimise both the MSE and NCC loss terms over all reconstructed input tokens.

## 4. Experiments & Results

### 4.1. Model Variants and Implementation Details

We introduce OTiS in three different configurations - Base, Large, and Huge (see Appendix C.1) - to explore scaling laws with respect to the model size. We set the patch size and stride to  $P = 24$ , respectively, to split the time series into  $T' = \frac{\bar{T}}{P}$  non-overlapping patches along the temporal dimension. For pre-training, the context length is set to  $\bar{T} = 1008$  time points, resulting in  $T' = 42$  sinusoidal temporal embeddings. If longer context lengths are required during fine-tuning, these embeddings are linearly interpolated (i.e.  $T'_n \geq 42$ ) to offer greater flexibility for downstream applications. We tune the hyperparameters for pre-training and fine-tuning as described in Appendix C. An overview of the computational costs is provided in Appendix D.

### 4.2. Large and Diverse Pre-Training Corpus

We aim to develop a general time series model that fully handles the heterogeneity in real-world data. Specifically, our model is designed to handle time series with different variate counts  $V_S$ , inter-variate relationships, temporal patterns, and sampling frequency, ensuring flexibility for downstream tasks. To this end, we pre-train our model on a large and diverse corpus of publicly available data spanning 8 domains, with a total of 640,187 samples and 11 billion time points, as summarised in Table 1. A detailed description of the datasets included in our pre-training corpus can be found in Appendix A. The time series corpus is split into 612,394

Table 2. Classification and regression results on a total of 9 benchmark tasks, with <sup>•</sup> indicating tasks in previously unseen domains. Best score in **bold**, second best underlined. OTiS successfully captures high-level semantics for classification and localised time series features for regression. Zero-shot and linear probing predictions indicate the generalisability of OTiS’ time series features.

(a) Classification [Accuracy (ACC  $\uparrow$ ) in %]

Model	Epilepsy	FD-B	Gesture <sup>•</sup>	EMG <sup>•</sup>
SimCLR 2020	90.71	49.17	48.04	61.46
TimesNet 2022a	94.01	56.86	59.79	91.22
CoST 2022	88.40	47.06	68.33	53.65
TS2Vec 2022	93.95	47.90	69.17	78.54
TF-C 2022	94.95	69.38	<u>76.42</u>	81.71
Ti-MAE 2023	89.71	60.88	71.88	69.99
SimMTM 2024	<b>95.49</b>	69.40	<b>80.00</b>	97.56
OTiS-Base	94.25	<b>99.24</b>	63.61	97.56
OTiS-Large	94.03	<u>98.62</u>	62.50	<u>98.37</u>
OTiS-Huge	91.48	<u>98.32</u>	63.61	<b>98.37</b>
OTiS <sub>0</sub> <sup>◦</sup>	<u>95.18</u>	61.32	51.67	95.12

<sup>◦</sup> Zero-shot predictions of OTiS-Base.

(b) Regression [R-squared ( $R^2$   $\uparrow$ )]

Model	LVEDV	LVESV	LVSV	LVEF	LVM
ViT 2021	0.409	0.396	0.299	0.175	0.469
MAE 2022	0.486	0.482	0.359	0.237	0.573
iTransformer 2023	0.307	0.279	0.227	0.070	0.361
CM-AE* 2023	0.451	0.380	0.316	0.103	0.536
MMCL* 2025	0.504	0.503	0.370	0.250	<b>0.608</b>
OTiS-Base	<b>0.509</b>	<u>0.512</u>	<b>0.391</b>	<b>0.292</b>	0.592
OTiS-Large	0.504	0.503	0.371	0.267	0.592
OTiS-Huge	<u>0.505</u>	<b>0.510</b>	<u>0.376</u>	<u>0.281</u>	<u>0.593</u>
OTiS <sub>LP</sub> <sup>◦</sup>	0.414	0.394	0.279	0.161	0.453

\* Models incorporate paired imaging data during pre-training.

<sup>◦</sup> Linear probing of OTiS-Base.

training and 27,793 validation samples for pre-training.

### 4.3. Benchmarking Across Domains and Tasks

We evaluate OTiS across general use cases in time series analysis: classification, regression, and forecasting. We use 12 datasets from 8 domains to compare our model against 27 baselines, as outlined in Appendix B. The baselines comprise 15 specialised, i.e. task-specific, models (either fully supervised or pre-trained and fine-tuned exclusively on target data) and 12 general models (pre-trained on external data and fine-tuned on target data), including 6 foundation models. We follow established data splitting and evaluation procedures for classification (Zhang et al., 2022), regression (Turgut et al., 2025), and forecasting (Zhou et al., 2021), with results reported across five seeds set during fine-tuning.

The experiments reveal that OTiS extracts powerful time series features, achieving state-of-the-art performance on 10

out of 15 diverse benchmarks. The classification results in Table 2a highlight its particular strength in processing long time series, yielding a huge performance boost on FD-B ( $\bar{T}_{\text{FD-B}} = 5112$ ). The regression results in Table 2b emphasise the effectiveness of pre-training across domains, with OTiS outperforming specialised models that are unimodally pre-trained (e.g. MAE) or even multimodally pre-trained (e.g. MMCL). This is further supported by an additional ablation study on different training strategies presented in Appendix G.2. Moreover, the forecasting results in Table 3 and Appendix H reveal that OTiS effectively captures temporal patterns and trends, even in previously unseen domains. Finally, zero-shot experiments detailed in Appendix F, along with experiments involving minimal training (e.g. linear probing or fine-tuning of domain-specific embeddings) in Table 2b and 3, highlight how the extracted time series features generalise across domains and tasks, e.g. evidenced by the Epilepsy, LVEDV, and ETTh2 benchmarks.

### 4.4. General Time Series Understanding

To evaluate whether OTiS has an intrinsic understanding of fundamental time series properties, such as frequency, amplitude, offset, and phase, we analyse *zero-shot* representations of sine waves, as illustrated in Figure 3. Particularly, we evaluate OTiS after pre-training without fine-tuning, using randomly initialised variate embeddings. We average the encoder’s output features to obtain a global representation.

When examining time series properties in isolation, we observe that their continuous variations are correctly mirrored in OTiS’ latent space. For frequency (see Figure 3a), the analysis reveals that embeddings for higher frequencies are positioned closer together, indicating greater similarity, than those for lower frequencies. This observation aligns with intuition: a change in frequency from 1 Hz to 50 Hz represents a factor of 50, thus resulting in more distinct embeddings, whereas a change from 50 Hz to 100 Hz reflects only a doubling of the frequency. Analogous patterns are observed for amplitude (see Figure 3b) and offset (see Figure 3c). In the case of phase (see Figure 3d), the latent space forms a closed circle, with embeddings for phases of 0 and  $2\pi$  being identical and positioned opposite to the embedding for a phase of  $\pi$ . These findings are consistent with the mathematical definition of a unit circle in the complex plane:

$$e^{i\phi} = \cos(\phi) + i\sin(\phi), \quad (7)$$

where  $\phi \in [0, 2\pi]$  denotes the phase. A phase of  $\phi = 2\pi$  corresponds to the identity (i.e.  $e^{i2\pi} = e^{i0}$ ), while  $\phi = \pi$  corresponds to a multiplication by  $-1$  (i.e.  $e^{i\pi} = -e^{i0}$ ).

Moreover, when faced with simultaneous variations in multiple time series properties (see Figure 3e), we observe that our model successfully disentangles them in its latent space. Overall, these findings demonstrate an intrinsic understand-

Table 3. Forecasting results on 6 benchmark tasks, with  $\circ$  indicating tasks in previously unseen domains. A forecasting horizon of 96 time points is predicted from the past 336 (\*512, +904) time points. Mean squared error (MSE  $\downarrow$ ) is reported. Best score in **bold**, second best underlined. OTiS successfully captures temporal patterns and trends essential for forecasting. Predictions involving minimal training ( $\circ$ ) indicate the generalisability of OTiS’ extracted time series features.

Model	ETTh1 $\circ$	ETTh2 $\circ$	ETTm1 $\circ$	ETTm2 $\circ$	Weather $\circ$	Electricity $\circ$
N-BEATS 2019	0.399	0.327	0.318	0.197	0.152	0.131
Autoformer 2021	0.435	0.332	0.510	0.205	0.249	0.196
TimesNet 2022a	0.384	0.340	0.338	0.187	0.172	0.168
DLinear 2023	0.375	0.289	0.299	0.167	0.176	0.140
PatchTST 2023	<b>0.370</b>	0.274	<u>0.293</u>	<u>0.166</u>	0.149	0.129
Time-LLM $\ddagger$ 2023	0.408	0.286	0.384	0.181	†	†
GPT4TS 2023	0.376	0.285	<b>0.292</b>	0.173	0.162	0.139
MOMENT* 2024	0.387	0.288	0.293	0.170	0.154	0.136
MOIRAI+ 2024	<u>0.375</u>	0.277	0.335	0.189	0.167	0.152
OTiS-Base	0.424	<u>0.212</u>	0.337	<b>0.161</b>	<b>0.139</b>	<u>0.128</u>
OTiS-Large	0.446	<b>0.205</b>	0.362	0.173	<u>0.142</u>	<b>0.127</b>
OTiS-Huge	0.461	0.215	0.384	0.181	0.149	0.132
OTiS <sub>VE</sub> $\circ$	0.434	0.214	0.396	0.174	0.149	0.164

† Experiments could not be conducted on a single NVIDIA RTX A6000-48GB GPU.

‡ Model incorporates paired text data during pre-training and fine-tuning.

$\circ$  Predictions of OTiS-Base with only the domain-specific variate embeddings (VE) being fine-tuned.

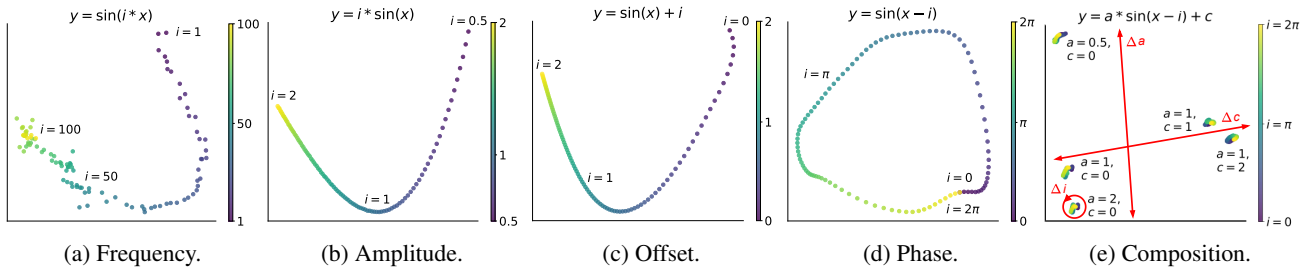


Figure 3. First two principal components of *zero-shot* sinusoidal representations extracted by OTiS-Base. We freeze OTiS after pre-training and use randomly initialised variate embeddings. The output features of the encoder are averaged to obtain a global representation. OTiS has an intrinsic understanding of fundamental time series properties, such as (a) frequency, (b) amplitude, (c) offset, and (d) phase. It effectively disentangles (e) simultaneous variations of these properties, providing a strong foundation for general time series analysis.

ing of fundamental time series properties, providing a strong and essential foundation for general time series analysis.

#### 4.5. Domain Signature Analysis

**Inter-Variate Relationships.** A key design choice of OTiS is the use of domain-specific variate embeddings. While these embeddings are randomly initialised, we expect them to capture unique domain characteristics, e.g. inter-variate relationships, during training. To test this hypothesis, we analyse the EEG-specific and ECG-specific variate embeddings learned during pre-training, and the Weather-specific variate embeddings learned during fine-tuning.

The principal component analysis (PCA) presented in Figure 7 (see Appendix E.2.1) demonstrates that EEG-specific variate embeddings accurately capture the 3D spatial arrangement of EEG electrodes placed on the human scalp. Similarly, the PCA in Figure 9 (see Appendix E.2.1) indi-

cates that ECG-specific variate embeddings correctly reflect the relationships among the 12 leads: limb leads I, II, and III form a planar 2D triangle, representing Einthoven’s triangle (Kligfield et al., 2007), while precordial leads V1–V6 capture a 3D view of the heart. Moreover, the embedding similarity analysis in Figure 10 (see Appendix E.2.1) reveals that Weather-specific variate embeddings capture the true physical relationships among climatological indicators. This also showcases that OTiS successfully adapts to previously unseen domains with limited data seen during fine-tuning.

**Temporal Patterns.** The central question is whether OTiS learns only the relationships across variates or also captures temporal patterns within a variate. To investigate this, we conduct forecasting experiments on uni-variate sine waves with distinct frequencies. Note that in a uni-variate setting ( $V_{\text{sine}} = 1$ ), we ensure that our model does not utilise information from other variates. For these experiments,

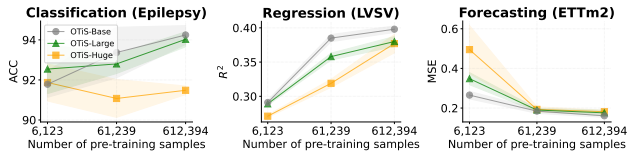


Figure 4. Scaling study. Shaded regions indicate the standard deviation across 5 seeds. Downstream performance across tasks generally scales with dataset size. Scaling the model size requires even larger pre-training corpora to be effective.

we freeze both the encoder  $f(\cdot)$  and decoder  $g(\cdot)$  after pre-training and fine-tune only a randomly initialised variate embedding  $\mathbf{E}_{\text{sine}}^V \in \mathbb{R}^{1 \times D}$  ( $< 0.2$ k trainable parameters) on 50 Hz sine waves. During inference, OTiS is fully frozen and forecasts are made on *unseen* sine waves with frequencies of 2 Hz, 28 Hz, 60 Hz, and 100 Hz. As shown in Figure 11 (see Appendix E.2.2), we find that the domain-specific variate embedding  $\mathbf{E}_{\text{sine}}^V$  captures temporal patterns that generalise to previously unseen frequencies. These observations demonstrate that OTiS learns not only the inter-variate relationships of a domain, but also its temporal patterns.

#### 4.6. Scaling Study

We analyse the scaling behaviour of OTiS with respect to dataset and model size. To this end, we subsample the pre-training data to 10% and 1% of its original size, ensuring that each subset is fully contained within the corresponding superset. We evaluate the downstream performance of all OTiS variants across classification, regression, and forecasting tasks, as depicted in Figure 4.

The experiments demonstrate that downstream performance generally scales with dataset size, achieving the best results with the full pre-training dataset. This trend, however, does not directly apply to model size, which is in line with the scaling behaviour observed in current time series foundation models (Woo et al., 2024; Goswami et al., 2024). Given that an increasing dataset size generally improves model performance, we hypothesise that scaling the model size could prove beneficial with even larger pre-training corpora.

#### 4.7. Ablation Study

We conduct an ablation study to analyse the impact of OTiS’ key components: the domain-specific tokeniser, dual masking strategy, and normalised cross-correlation (NCC) loss. As shown in Figure 5, OTiS achieves superior performance when all components are integrated during pre-training.

Replacing domain-specific variate embeddings with domain-agnostic ones (i.e. variate embeddings shared across all domains) consistently led to inferior performance across tasks, indicating the importance of considering domain characteristics during tokenisation. Switching from dual to random

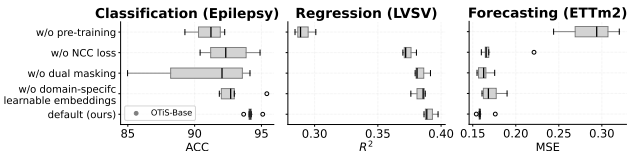


Figure 5. Ablation study. Downstream performance is analysed across 5 seeds. A leave-one-out approach is used to evaluate the influence of each component. The default setup, incorporating all components, achieves superior performance across tasks.

masking resulted in performance degradation, although the impact was less notable for generative tasks than for discriminative tasks. We hypothesise that the NCC loss already captures temporal causality, which is particularly helpful for generative tasks like forecasting. Overall, removing the NCC loss caused performance declines across all downstream applications, emphasising the importance of long-range dependencies for general time series understanding.

## 5. Discussion & Conclusion

In this study, we explore the problem of efficient pre-training on heterogeneous time series corpora. Prevalent in domains ranging from medicine to finance, time series vary notably e.g with respect to inter-variate relationships and temporal patterns, rendering efficient pre-training across domains difficult. To address this, we propose a novel pre-training paradigm including a tokeniser with learnable domain signatures, a dual masking strategy, and a normalised cross-correlation loss, enabling our **open** model for general time series analysis (OTiS) to learn general time series features.

In extensive benchmarking experiments, OTiS is competitive against specialised state-of-the-art (SoTA) models. Our qualitative analysis highlights how learnable domain signatures address time series heterogeneity, facilitating the disentanglement of domain-specific knowledge and enabling OTiS to acquire knowledge on fundamental time series properties shared across domains, such as frequency, amplitude, offset, or phase. This is particularly valuable in domains with limited data availability and high privacy standards, such as medicine, where our approach offers a promising solution by leveraging readily available data from any domain. Overall, our work establishes an essential foundation for future advancements in time series analysis.

**Limitations.** While OTiS outperforms SoTA models across diverse tasks, scaling studies indicate that larger pre-training corpora could further benefit performance. Unlike in NLP and CV, where large corpora are curated from the web, time series foundation models, including OTiS, still rely on manually curated data. Future work could explore fully automated pipelines to filter time series from the web



and categorise them into domains, e.g. using embedding similarities. Finally, integrating other modalities, such as imaging or text, is a promising direction for future research.

## Impact Statement

This paper presents work whose goal is to advance the field of Machine Learning. There are many potential societal consequences of our work, none which we feel must be specifically highlighted here.

## References

- Alabdulmohsin, I., Neyshabur, B., and Zhai, X. Revisiting neural scaling laws in language and vision. In *Advances in Neural Information Processing Systems*, 2022.
- Andrzejak, R. G., Lehnertz, K., Mormann, F., Rieke, C., David, P., and Elger, C. E. Indications of nonlinear deterministic and finite-dimensional structures in time series of brain electrical activity: Dependence on recording region and brain state. *Physical Review E*, 2001.
- Babayan, A., Erbey, M., Kumral, D., Reinelt, J. D., Reiter, A. M., Röbbing, J., Schaare, H. L., Uhlig, M., Anwender, A., Bazin, P.-L., et al. A mind-brain-body dataset of mri, eeg, cognition, emotion, and peripheral physiology in young and old adults. *Scientific data*, 2019.
- Bai, W., Suzuki, H., Huang, J., Francis, C., Wang, S., Tarroni, G., Guitton, F., Aung, N., Fung, K., Petersen, S. E., et al. A population-based phenome-wide association study of cardiac and aortic structure and function. *Nature Medicine*, 2020.
- Cherti, M., Beaumont, R., Wightman, R., Wortsman, M., Ilharco, G., Gordon, C., Schuhmann, C., Schmidt, L., and Jitsev, J. Reproducible scaling laws for contrastive language-image learning. In *IEEE/CVF Conference on Computer Vision and Pattern Recognition*, 2023.
- Chowdhery, A., Narang, S., Devlin, J., Bosma, M., Mishra, G., Roberts, A., Barham, P., Chung, H. W., Sutton, C., Gehrmann, S., et al. Palm: Scaling language modeling with pathways. *Journal of Machine Learning Research*, 2023.
- Das, A., Kong, W., Sen, R., and Zhou, Y. A decoder-only foundation model for time-series forecasting. In *International Conference on Machine Learning*, 2024.
- Dong, J., Wu, H., Zhang, H., Zhang, L., Wang, J., and Long, M. Simmtm: A simple pre-training framework for masked time-series modeling. In *Advances in Neural Information Processing Systems*, 2024.
- Dosovitskiy, A., Beyer, L., Kolesnikov, A., Weissenborn, D., Zhai, X., Unterthiner, T., Dehghani, M., Minderer, M., Heigold, G., Gelly, S., Uszkoreit, J., and Houshy, N. An image is worth 16x16 words: Transformers for image recognition at scale. In *International Conference on Learning Representations*, 2021.
- Einthoven, W., Jaffe, A., Venge, P., and Lindahl, B. Galvanometrische registratie van het menselijk electrocardiogram. *Herinneringsbundel Professor SS Rosenstein*, 1902.
- Fawaz, H. I., Forestier, G., Weber, J., Idoumghar, L., and Muller, P.-A. Transfer learning for time series classification. In *IEEE International Conference on Big Data*, 2018.
- Gasparin, A., Lukovic, S., and Alippi, C. Deep learning for time series forecasting: The electric load case. *CAAI Transactions on Intelligence Technology*, 2022.
- Geirhos, R., Rubisch, P., Michaelis, C., Bethge, M., Wichmann, F. A., and Brendel, W. Imagenet-trained cnns are biased towards texture; increasing shape bias improves accuracy and robustness. *International Conference on Learning Representations*, 2019.
- Gemmeke, J. F., Ellis, D. P., Freedman, D., Jansen, A., Lawrence, W., Moore, R. C., Plakal, M., and Ritter, M. Audio set: An ontology and human-labeled dataset for audio events. In *IEEE International Conference on Acoustics, Speech and Signal Processing (ICASSP)*, 2017.
- Goldberger, E. A simple, indifferent, electrocardiographic electrode of zero potential and a technique of obtaining augmented, unipolar, extremity leads. *American Heart Journal*, 1942.
- Gordon, M. A., Duh, K., and Kaplan, J. Data and parameter scaling laws for neural machine translation. In *Conference on Empirical Methods in Natural Language Processing*, 2021.
- Goswami, M., Szafer, K., Choudhry, A., Cai, Y., Li, S., and Dubrawski, A. Moment: A family of open time-series foundation models. *International Conference on Machine Learning*, 2024.
- Gow, B., Pollard, T., Nathanson, L. A., Johnson, A., Moody, B., Fernandes, C., Greenbaum, N., Berkowitz, S., Moukheiber, D., Eslami, P., et al. Mimic-iv-ecg-diagnostic electrocardiogram matched subset. *PyhsioNet*, 2023.
- Gupta, P., Malhotra, P., Narwariya, J., Vig, L., and Shroff, G. Transfer learning for clinical time series analysis using deep neural networks. *Journal of Healthcare Informatics Research*, 2020.

- He, K., Chen, X., Xie, S., Li, Y., Dollár, P., and Girshick, R. Masked autoencoders are scalable vision learners. In *IEEE/CVF Conference on Computer Vision and Pattern Recognition*, 2022.
- Homan, R. W., Herman, J., and Purdy, P. Cerebral location of international 10–20 system electrode placement. *Electroencephalography and clinical neurophysiology*, 1987.
- Ismail Fawaz, H., Forestier, G., Weber, J., Idoumghar, L., and Muller, P.-A. Deep learning for time series classification: a review. *Data Mining and Knowledge Discovery*, 2019.
- Iwana, B. K. and Uchida, S. An empirical survey of data augmentation for time series classification with neural networks. *Plos one*, 2021.
- Jiang, W., Zhao, L., and liang Lu, B. Large brain model for learning generic representations with tremendous EEG data in BCI. In *International Conference on Learning Representations*, 2024.
- Jin, M., Wang, S., Ma, L., Chu, Z., Zhang, J. Y., Shi, X., Chen, P.-Y., Liang, Y., Li, Y.-F., Pan, S., et al. Time-llm: Time series forecasting by reprogramming large language models. *International Conference on Learning Representations*, 2023.
- Jing, J., Ge, W., Hong, S., Fernandes, M. B., Lin, Z., Yang, C., An, S., Struck, A. F., Herlopian, A., Karakis, I., et al. Development of expert-level classification of seizures and rhythmic and periodic patterns during eeg interpretation. *Neurology*, 2023.
- Jurcak, V., Tsuzuki, D., and Dan, I. 10/20, 10/10, and 10/5 systems revisited: their validity as relative head-surface-based positioning systems. *Neuroimage*, 2007.
- Kaplan, J., McCandlish, S., Henighan, T., Brown, T. B., Chess, B., Child, R., Gray, S., Radford, A., Wu, J., and Amodei, D. Scaling laws for neural language models. *arXiv preprint arXiv:2001.08361*, 2020.
- Kemp, B., Zwinderman, A. H., Tuk, B., Kamphuisen, H. A., and Obery, J. J. Analysis of a sleep-dependent neuronal feedback loop: the slow-wave microcontinuity of the eeg. *IEEE Transactions on Biomedical Engineering*, 2000.
- Kligfield, P., Gettes, L. S., Bailey, J. J., Childers, R., Deal, B. J., Hancock, E. W., Van Herpen, G., Kors, J. A., Macfarlane, P., Mirvis, D. M., et al. Recommendations for the standardization and interpretation of the electrocardiogram: part i: the electrocardiogram and its technology: a scientific statement from the american heart association electrocardiography and arrhythmias committee, council on clinical cardiology; the american college of cardiology foundation; and the heart rhythm society endorsed by the international society for computerized electrocardiology. *Circulation*, 2007.
- Kreuzer, D., Beaini, D., Hamilton, W., Létourneau, V., and Tossou, P. Rethinking graph transformers with spectral attention. *Advances in Neural Information Processing Systems*, 2021.
- Lai, G., Chang, W.-C., Yang, Y., and Liu, H. Modeling long-and short-term temporal patterns with deep neural networks. In *International ACM SIGIR conference on research & development in information retrieval*, 2018.
- Lessmeier, C., Kimotho, J. K., Zimmer, D., and Sextro, W. Condition monitoring of bearing damage in electromechanical drive systems by using motor current signals of electric motors: A benchmark data set for data-driven classification. In *PHM Society European Conference*, 2016.
- Li, H., Ding, M., Zhang, R., and Xiu, C. Motor imagery eeg classification algorithm based on cnn-lstm feature fusion network. *Biomedical signal processing and control*, 2022.
- Li, Z., Rao, Z., Pan, L., Wang, P., and Xu, Z. Ti-mae: Self-supervised masked time series autoencoders. *arXiv preprint arXiv:2301.08871*, 2023.
- Liu, J., Zhong, L., Wickramasuriya, J., and Vasudevan, V. uwave: Accelerometer-based personalized gesture recognition and its applications. *Pervasive and Mobile Computing*, 2009.
- Liu, Y., Hu, T., Zhang, H., Wu, H., Wang, S., Ma, L., and Long, M. itransformer: Inverted transformers are effective for time series forecasting. *International Conference on Learning Representations*, 2023.
- Liu, Y., Zhang, H., Li, C., Huang, X., Wang, J., and Long, M. Timer: Generative pre-trained transformers are large time series models. *International Conference on Machine Learning*, 2024.
- McCracken, M. W. and Ng, S. Fred-md: A monthly database for macroeconomic research. *Journal of Business & Economic Statistics*, 2016.
- Nie, Y., Nguyen, N. H., Sinthong, P., and Kalagnanam, J. A time series is worth 64 words: Long-term forecasting with transformers. In *International Conference on Learning Representations*, 2023.
- Obeid, I. and Picone, J. The temple university hospital eeg data corpus. *Frontiers in neuroscience*, 2016.
- Oquab, M., Darcet, T., Moutakanni, T., Vo, H. V., Szafraniec, M., Khalidov, V., Fernandez, P., HAZIZA,

- D., Massa, F., El-Nouby, A., Assran, M., Ballas, N., Galuba, W., Howes, R., Huang, P.-Y., Li, S.-W., Misra, I., Rabbat, M., Sharma, V., Synnaeve, G., Xu, H., Jegou, H., Mairal, J., Labatut, P., Joulin, A., and Bojanowski, P. DINOv2: Learning robust visual features without supervision. *Transactions on Machine Learning Research*, 2024.
- Oreshkin, B. N., Carпов, D., Chapados, N., and Bengio, Y. N-beats: Neural basis expansion analysis for interpretable time series forecasting. *International Conference on Learning Representations*, 2019.
- Peh, W. Y., Yao, Y., and Dauwels, J. Transformer convolutional neural networks for automated artifact detection in scalp eeg. In *2022 44th Annual International Conference of the IEEE Engineering in Medicine & Biology Society (EMBC)*, 2022.
- PhysioBank, P. Physionet: components of a new research resource for complex physiologic signals. *Circulation*, 2000.
- Pirkis, J., John, A., Shin, S., DelPozo-Banos, M., Arya, V., Analuisa-Aguilar, P., Appleby, L., Arensman, E., Bantjes, J., Baran, A., et al. Suicide trends in the early months of the covid-19 pandemic: an interrupted time-series analysis of preliminary data from 21 countries. *The Lancet Psychiatry*, 2021.
- Radford, A., Narasimhan, K., Salimans, T., Sutskever, I., et al. Improving language understanding by generative pre-training. *OpenAI*, 2018.
- Radhakrishnan, A., Friedman, S. F., Khurshid, S., Ng, K., Batra, P., Lubitz, S. A., Philippakis, A. A., and Uhler, C. Cross-modal autoencoder framework learns holistic representations of cardiovascular state. *Nature Communications*, 2023.
- Ravi, N., Gabeur, V., Hu, Y.-T., Hu, R., Ryali, C., Ma, T., Khedr, H., Rädle, R., Rolland, C., Gustafson, L., et al. Sam 2: Segment anything in images and videos. *arXiv preprint arXiv:2408.00714*, 2024.
- Ravuri, S., Lenc, K., Willson, M., Kangin, D., Lam, R., Mirowski, P., Fitzsimons, M., Athanassiadou, M., Kashem, S., Madge, S., et al. Skilful precipitation nowcasting using deep generative models of radar. *Nature*, 2021.
- Schoffelen, J.-M. and Gross, J. Source connectivity analysis with meg and eeg. *Human brain mapping*, 2009.
- Sezer, O. B., Gudelek, M. U., and Ozbayoglu, A. M. Financial time series forecasting with deep learning: A systematic literature review: 2005–2019. *Applied Soft Computing*, 2020.
- Song, Y., Jia, X., Yang, L., and Xie, L. Transformer-based spatial-temporal feature learning for eeg decoding. *arXiv preprint arXiv:2106.11170*, 2021.
- Sudlow, C., Gallacher, J., Allen, N., Beral, V., Burton, P., Danesh, J., Downey, P., Elliott, P., Green, J., Landray, M., Liu, B., Matthews, P., Ong, G., Pell, J., Silman, A., Young, A., Sprosen, T., Peakman, T., and Collins, R. UK biobank: an open access resource for identifying the causes of a wide range of complex diseases of middle and old age. *PLoS Medicine*, 2015.
- Taieb, S. B., Bontempi, G., Atiya, A. F., and Sorjamaa, A. A review and comparison of strategies for multi-step ahead time series forecasting based on the nn5 forecasting competition. *Expert Systems with Applications*, 2012.
- Tang, C. I., Perez-Pozuelo, I., Spathis, D., and Mascolo, C. Exploring contrastive learning in human activity recognition for healthcare. *arXiv preprint arXiv:2011.11542*, 2020.
- Touvron, H., Lavril, T., Izacard, G., Martinet, X., Lachaux, M.-A., Lacroix, T., Rozière, B., Goyal, N., Hambro, E., Azhar, F., et al. Llama: Open and efficient foundation language models. *arXiv preprint arXiv:2302.13971*, 2023.
- Turgut, Ö., Müller, P., Hager, P., Shit, S., Starck, S., Menten, M. J., Martens, E., and Rueckert, D. Unlocking the diagnostic potential of electrocardiograms through information transfer from cardiac magnetic resonance imaging. *Medical Image Analysis*, 2025.
- UCI. Uci electricity load time series dataset. *UCI*, 2024. <https://archive.ics.uci.edu/dataset/321/electricityloaddiagrams20112014>.
- Van Dijk, H., Van Wingen, G., Denys, D., Olbrich, S., Van Ruth, R., and Arns, M. The two decades brainclinics research archive for insights in neurophysiology (tdbrain) database. *Scientific data*, 2022.
- Vaswani, A., Shazeer, N., Parmar, N., Uszkoreit, J., Jones, L., Gomez, A. N., Kaiser, Ł., and Polosukhin, I. Attention is all you need. *Advances in Neural Information Processing Systems*, 30, 2017.
- Wetterdienst, D. Temperature dataset. *DWD*, 2024. <https://www.dwd.de/DE/leistungen/klimadatendeutschland/klarchivtagmonat.html>.
- Wetterstation. Weather dataset. *Wetter*, 2024. <https://www.bgc-jena.mpg.de/wetter/>.
- Wickstrøm, K., Kampffmeyer, M., Mikalsen, K. Ø., and Jenssen, R. Mixing up contrastive learning: Self-supervised representation learning for time series. *Pattern Recognition Letters*, 2022.

- Wilson, F. N., Johnston, F. D., Macleod, A. G., and Barker, P. S. Electrocardiograms that represent the potential variations of a single electrode. *American Heart Journal*, 1934.
- Woo, G., Liu, C., Sahoo, D., Kumar, A., and Hoi, S. CoST: Contrastive learning of disentangled seasonal-trend representations for time series forecasting. In *International Conference on Learning Representations*, 2022.
- Woo, G., Liu, C., Kumar, A., Xiong, C., Savarese, S., and Sahoo, D. Unified training of universal time series forecasting transformers. *International Conference on Machine Learning*, 2024.
- Wu, H., Xu, J., Wang, J., and Long, M. Autoformer: Decomposition transformers with auto-correlation for long-term series forecasting. In *Advances in Neural Information Processing Systems*, 2021.
- Wu, H., Hu, T., Liu, Y., Zhou, H., Wang, J., and Long, M. Timesnet: Temporal 2d-variation modeling for general time series analysis. In *International Conference on Learning Representations*, 2022a.
- Wu, X., Zheng, W.-L., Li, Z., and Lu, B.-L. Investigating eeg-based functional connectivity patterns for multi-modal emotion recognition. *Journal of neural engineering*, 2022b.
- Yang, C., Xiao, C., Westover, M. B., Sun, J., et al. Self-supervised electroencephalogram representation learning for automatic sleep staging: model development and evaluation study. *JMIR AI*, 2023.
- Yang, C., Westover, M., and Sun, J. Biot: Biosignal transformer for cross-data learning in the wild. *Advances in Neural Information Processing Systems*, 2024.
- Ye, R. and Dai, Q. Implementing transfer learning across different datasets for time series forecasting. *Pattern Recognition*, 2021.
- Yue, Z., Wang, Y., Duan, J., Yang, T., Huang, C., Tong, Y., and Xu, B. Ts2vec: Towards universal representation of time series. In *AAAI Conference on Artificial Intelligence*, 2022.
- Zeng, A., Chen, M., Zhang, L., and Xu, Q. Are transformers effective for time series forecasting? In *AAAI Conference on Artificial Intelligence*, 2023.
- Zhang, X., Zhao, Z., Tsiligkaridis, T., and Zitnik, M. Self-supervised contrastive pre-training for time series via time-frequency consistency. *Advances in Neural Information Processing Systems*, 2022.
- Zhang, Z.-M., Chen, S., and Liang, Y.-Z. Baseline correction using adaptive iteratively reweighted penalized least squares. *Analyst*, 2010.
- Zheng, W.-L. and Lu, B.-L. Investigating critical frequency bands and channels for EEG-based emotion recognition with deep neural networks. *IEEE Transactions on Autonomous Mental Development*, 2015.
- Zhou, H., Zhang, S., Peng, J., Zhang, S., Li, J., Xiong, H., and Zhang, W. Informer: Beyond efficient transformer for long sequence time-series forecasting. In *AAAI Conference on Artificial Intelligence*, 2021.
- Zhou, J., Wei, C., Wang, H., Shen, W., Xie, C., Yuille, A., and Kong, T. Image BERT pre-training with online tokenizer. In *International Conference on Learning Representations*, 2022.
- Zhou, T., Niu, P., Sun, L., Jin, R., et al. One fits all: Power general time series analysis by pretrained lm. *Advances in neural information processing systems*, 2023.

## A. Large Multi-Domain Pre-Training Corpus

In this section, we present an overview of our large and diverse pre-training corpus. The corpus consists of publicly available data spanning eight domains, with a total of 640,187 samples and 11 billion time points. In the following, we provide a detailed breakdown of the domains and the datasets they encompass. Note that we apply channel-wise standard normalisation to the datasets unless otherwise specified.

**ECG.** The MIMIC-IV-ECG dataset (Gow et al., 2023) contains diagnostic 10-second, 12-lead ECG recordings sampled at a frequency of 500 Hz. While the entire dataset comprises 800,035 samples, we include only the first half of the recordings available in the database, preventing the ECG data from predominating in the pre-training corpus. To remove the baseline drift from the ECG data, we use the asymmetric least square smoothing technique (Zhang et al., 2010). Note that we apply standard normalisation separately to the Einthoven, Goldberger, and Wilson leads.

**Temperature.** The Deutscher Wetterdienst (DWD) dataset (Wetterdienst, 2024) contains hourly air temperature measurements from 629 weather stations across Germany. Since the recording length varies significantly, ranging from 763 to 1,148,290 hours per station, we split the data into chunks of 720 hours (approximately one month).

**Audio.** The AudioSet dataset (Gemmeke et al., 2017) contains 10-second YouTube clips for audio classification, featuring 527 types of audio events that are weakly annotated for each clip. The full training set includes a class-wise balanced subset (AudioSet-20K, 22,176 clips) and an unbalanced (AudioSet-2M 2,042,985 clips) set. For our pre-training corpus, we use the balanced AudioSet-20K, which contains 3,491 mono and 16,123 stereo recordings, all sampled at 44.1 kHz.

**Electromechanics.** The FD-A dataset (Lessmeier et al., 2016) collects vibration signals from rolling bearings in a mechanical system for fault detection purposes. Each sample consists of 5,120 timestamps, indicating one of three mechanical device states. Note that the FD-B dataset is similar to FD-A but includes rolling bearings tested under different working conditions, such as varying rotational speeds.

**EEG.** The TDBrain dataset (Van Dijk et al., 2022) includes raw resting-state EEG data from 1,274 psychiatric patients aged 5 to 89, collected between 2001 and 2021. The dataset covers a range of conditions, including Major Depressive Disorder (426 patients), Attention Deficit Hyperactivity Disorder (271 patients), Subjective Memory Complaints (119 patients), and Obsessive-Compulsive Disorder (75 patients). The data was recorded at 500 Hz using 26 channel EEG-recordings, based on the 10-10 electrode international system.

The SEED dataset (Zheng & Lu, 2015) contains EEG data recorded under three emotional states: positive, neutral, and negative. It comprises EEG data from 15 subjects, with each subject participating in experiments twice, several days apart. The data is sampled at 200 Hz and recorded using 62 channel EEG-recordings, based on the 10-20 electrode international system.

For simplicity, we only consider the 19 channels common to both datasets, i.e. the channels that correspond to the 10-20 electrode international system.

**Banking.** The NN5 competition dataset (Taieb et al., 2012) consists of daily cash withdrawals observed at 111 randomly selected automated teller machines across various locations in England.

**Economics.** The FRED-MD dataset (McCracken & Ng, 2016) contains 107 monthly time series showing a set of macro-economic indicators from the Federal Reserve Bank of St Louis. The data was extracted from the FRED-MD database.

The Exchange dataset (Lai et al., 2018) records the daily exchange rates of eight different nations, including Australia, Great Britain, Canada, Switzerland, China, Japan, New Zealand, and Singapore, ranging from 1990 to 2016.

## B. Benchmark Details

To assess the utility of OTIS in real-world settings, we conduct experiments on three key use cases in time series analysis: classification, regression, and forecasting. For classification, we perform binary epilepsy detection using EEG

Table 4. Summary of all datasets used for benchmarking, including evaluation metrics, domains, and dataset details.

Task	Metric	Dataset						
		Domain $S$	Name	Samples	Variates $V_S$	Time points	Frequency	
Classification	ACC	EEG	Epilepsy 2001	11,500	1	178	174 Hz	
			TUEV 2016	112,237	19	1,000	200 Hz	
		Electromechanics Acceleration	FD-B 2016	13,640	1	5,120	64 kHz	
			Gesture 2009	560	3	206	100 Hz	
		EMG	EMG 2000	204	1	1,500	4 kHz	
Regression	$R^2$	ECG	UK BioBank 2015	18,926	12	5,000	500 Hz	
Forecasting	MSE	Energy	ETTh1 2021	1	7	17,420	(hourly) 278 $\mu$ Hz	
			ETTh2 2021	1	7	17,420	(hourly) 278 $\mu$ Hz	
			ETTh1 2021	1	7	69,680	(minutely) 1.1 mHz	
			ETTh2 2021	1	7	69,680	(minutely) 1.1 mHz	
			Weather	Weather 2024	1	21	52,696	(minutely) 2.8 mHz
			Electricity	Electricity 2024	321	1	26,304	(hourly) 278 $\mu$ Hz

(Epilepsy 2001), multi-class fault detection in rolling bearings from vibration signals (FD-B 2016), multi-class hand-gesture classification with accelerometer signals (Gesture 2009), and multi-class muscular disease classification using electromyographie (EMG 2000). For regression, we predict five imaging-derived cardiac phenotypes from 12-lead ECG (LVEDV, LVESV, LVSV, LVEF, LVM 2020). For forecasting, we predict electricity transformer temperature (ETT 2021), weather (Weather 2024), and electricity consumption (Electricity 2024). We adhere to the established data splitting and evaluation procedures for the classification (Zhang et al., 2022), regression (Turgut et al., 2025), and forecasting (Zhou et al., 2021) tasks. We provide an overview of the datasets and baselines used to benchmark our model in Table 4 and Table 5, respectively.

## C. Experiment Details

### C.1. Model Variants

To explore the scaling laws with respect to the model size, we provide OTiS in three variants, as summarised in Table 6.

### C.2. Pre-Training & Fine-Tuning Parameters

We provide the hyperparameters used to pre-train all variants of OTiS in Table 7. The hyperparameters used to fine-tune our models for the classification, regression, and forecasting tasks are provided in Table 8, 9, and 10, respectively.

## D. Computation Costs

We provide an overview of the computational resources used to train OTiS in Table 11.

## E. Domain Signature Analysis

We analyse the domain signatures, i.e. the domain-specific variate embeddings, by employing a principal component analysis (PCA) and embedding similarity analysis. Our analyses show that OTiS unifies time series from diverse domains into a meaningful latent space (see Section E.1), while accurately capturing the inter-variate relationships (see Section E.2.1) and temporal patterns within a domain (see Section E.2.2).

Table 5. Summary of all baseline models used for benchmarking, including pre-training details, domain adaptation methods, and architectural design. CL, MDM, and GPT denote contrastive learning, masked data modelling, and generative pre-training, respectively.

Task	Model	Pre-training		Domain adaptation	Architecture
		Method	Dataset		
Classification	SimCLR 2020	CL	SleepEEG* 2000	Fine-tuning	1D-CNN
	TimesNet 2022a	–	–	Fine-tuning	2D-CNN
	CoST 2022	CL	SleepEEG* 2000	Fine-tuning	1D-CNN
	TS2Vec 2022	CL	SleepEEG* 2000	Fine-tuning	1D-CNN
	TF-C 2022	CL	SleepEEG* 2000	Fine-tuning	Transformer
	Ti-MAE 2023	MDM	SleepEEG* 2000	Fine-tuning	Transformer
	SimMTM 2024	MDM	SleepEEG* 2000	Fine-tuning	Transformer
	ST-Transformer 2021	–	–	Fine-tuning	Transformer
	CNN-Transformer 2022	–	–	Fine-tuning	CNN w/ Transformer
	FFCL 2022	–	–	Fine-tuning	CNN w/ LSTM
	SPaRCNet 2023	–	–	Fine-tuning	1D-CNN
	ContraWR 2023	CL	Target	Fine-tuning	Transformer
	BIOT 2024	MDM	+	Fine-tuning	Transformer
	LaBraM 2024	MDM	□	Fine-tuning	Transformer
Regression	iTransformer 2023	–	–	Fine-tuning	Transformer
	ViT 2025	–	–	Fine-tuning	Transformer
	MAE 2025	MDM	Target	Fine-tuning	Transformer
	CM-AE 2023	MDM and CL	Target	Fine-tuning	1D-CNN
	MMCL 2025	MDM and CL	Target	Fine-tuning	Transformer
Forecasting	N-BEATS 2019	–	–	Fine-tuning	Non-Linear Model
	Autoformer 2021	–	–	Fine-tuning	Transformer
	TimesNet 2022a	–	–	Fine-tuning	2D-CNN
	DLinear 2023	–	–	Fine-tuning	Linear Model
	PatchTST 2023	MDM	Target	Fine-tuning	Transformer
	Time-LLM 2023	GPT	†	Fine-tuning	Transformer
	GPT4TS 2023	GPT	‡	Fine-tuning	Transformer
	MOMENT 2024	MDM	TSP <sup>°</sup> 2024	Fine-tuning	Transformer
	MOIRAI 2024	MDM	LOTSAs <sup>∠</sup> 2024	Zero-shot	Transformer

\* 371, 055 uni-variate, 2-seconds EEG recordings sampled at a frequency of 100 Hz.

+ Pre-training corpus spans 6 EEG datasets with more than 5 million samples and 13, 000 recording hours

□ Pre-training corpus spans 16 EEG datasets with a total of 2, 500 recording hours

† Model uses Llama-7B 2023, pre-trained on 1.4 trillion text tokens, as encoder.

‡ Model uses GPT2 2018, pre-trained on 10 billion text tokens, as encoder.

° Time Series Pile (TSP) contains 13 million samples and 1.23 billion time points from 13 domains.

∠ Large-Scale Open Time Series Archive (LOTSAs) contains more than 4 million samples and 27 billion time points from 9 domains.

Table 6. Details of model variants.

Model	Layers	Hidden size $D$	MLP size	Heads	$d_{kv}$	Parameters
OTiS-Base	12	192	768	3	64	8 M
OTiS-Large	18	384	1536	6	64	44 M
OTiS-Huge	24	576	2304	8	72	131 M

### E.1. Inter-Domain Analysis

A visualisation of all domain-specific variate embeddings learned during pre-training is provided in Figure 6. OTiS learns a meaningful latent space, where embeddings of domains with shared high-level semantics cluster closely together.

Table 7. Hyperparameters used for pre-training. Pre-training is performed on 4 NVIDIA A100-80GB GPUs. A cosine learning rate scheduler is applied with a 10% warmup. All OTiS configurations use a shallow decoder with 2M parameters, consisting of 4 layers with a hidden size of 160, an MLP with size 640, and 5 heads.

Model	Epochs	Batch size	Base LR	LR decay	NCC $\lambda$	Mask ratio $\rho$	Weight decay
OTiS-Base	200	5120	3e-5	cosine	0.1	0.75	0.10
OTiS-Large	200	3328	1e-5	cosine	0.1	0.75	0.15
OTiS-Huge	200	2880	3e-6	cosine	0.1	0.75	0.05

Table 8. Hyperparameters used for fine-tuning the classification tasks on a single NVIDIA RTX A6000-48GB GPU. A cosine learning rate scheduler is applied with a 10% warmup.

Dataset	Model	Epochs	Batch size	Base LR	Drop path	Layer decay	Weight decay	Label smoothing
Epilepsy	OTiS-Base	75	32	1e-3	0.2	0.75	0.2	0.1
	OTiS-Large	75	32	3e-3	0.2	0.50	0.1	0.1
	OTiS-Huge	75	32	3e-3	0.0	0.75	0.2	0.2
FD-B	OTiS-Base	75	32	3e-4	0.0	0.75	0.1	0.1
	OTiS-Large	75	32	1e-3	0.1	0.75	0.1	0.2
	OTiS-Huge	75	32	3e-4	0.1	0.75	0.2	0.1
Gesture	OTiS-Base	75	32	3e-3	0.2	0.50	0.1	0.1
	OTiS-Large	75	32	3e-3	0.2	0.75	0.1	0.0
	OTiS-Huge	75	32	1e-2	0.0	0.75	0.1	0.1
EMG	OTiS-Base	75	32	1e-3	0.2	0.75	0.1	0.2
	OTiS-Large	75	32	3e-3	0.1	0.75	0.2	0.1
	OTiS-Huge	75	32	3e-3	0.1	0.75	0.2	0.2

Table 9. Hyperparameters used for fine-tuning the regression tasks on a single NVIDIA RTX A6000-48GB GPU. A cosine learning rate scheduler is applied with a 10% warmup.

Dataset	Model	Epochs	Batch size	Base LR	Drop path	Layer decay	Weight decay
UK BioBank	OTiS-Base	50	192	3e-4	0.2	0.75	0.1
	OTiS-Large	50	160	1e-4	0.2	0.75	0.1
	OTiS-Huge	50	200	1e-4	0.2	0.75	0.1

## E.2. Intra-Domain Analysis

### E.2.1. INTER-VARIATE RELATIONSHIPS

**EEG-Specific Variate Embeddings.** In medicine, an electroencephalography (EEG) is used to record brain activity via electrodes attached to the scalp. The spatial arrangement of these electrodes is defined by established protocols, such as the international 10-20 system for EEG recordings (Homan et al., 1987). Hence, in an EEG recording, each variate corresponds to the brain activity captured by a single electrode with a well-defined spatial position. We hypothesise that the spatial arrangement of these electrodes is recoverable from the EEG-specific variate embeddings, assuming that recordings from electrodes in close proximity exhibit higher correlations than those from electrodes placed farther apart. To test this hypothesis, we analyse the latent space of EEG-specific variate embeddings learned during pre-training and fine-tuning, as described in the following.

Assume 3D electrode coordinates of the international 10-20 system for EEG recordings (Homan et al., 1987) to be defined in Euclidean space  $\mathbb{E}_Y^3$ . (see Figure 7a). We first determine the first three principal components of the EEG-specific variate embeddings, thus projecting them into a Euclidean space  $\mathbb{E}_X^3$  (see Figure 7b). Then, we perform a multivariate linear



Table 10. Hyperparameters used for fine-tuning the forecasting tasks. A cosine learning rate scheduler is applied with a 10% warmup.

Dataset	Model	Epochs	Batch size	Base LR	NCC $\lambda$	Weight decay
ETTh1	OTiS-Base	1000	1	3e-2	0.1	0.15
	OTiS-Large	1000	1	3e-3	0.2	0.15
	OTiS-Huge	1000	1	1e-2	0.1	0.15
ETTh2	OTiS-Base	1000	1	3e-2	0.2	0.25
	OTiS-Large	1000	1	3e-3	0.1	0.25
	OTiS-Huge	1000	1	1e-2	0.0	0.25
ETTm1	OTiS-Base	1000	1	1e-2	0.2	0.25
	OTiS-Large	1000	1	1e-2	0.2	0.25
	OTiS-Huge	1000	1	3e-3	0.1	0.15
ETTm2	OTiS-Base	1000	1	1e-2	0.1	0.25
	OTiS-Large	1000	1	3e-3	0.2	0.25
	OTiS-Huge	1000	1	1e-2	0.2	0.25
Weather	OTiS-Base	1000	1	1e-2	0.2	0.25
	OTiS-Large	1000	1	1e-2	0.2	0.15
	OTiS-Huge	1000	1	3e-3	0.2	0.05
Electricity	OTiS-Base	250	32	1e-3	0.0	0.25
	OTiS-Large	250	32	1e-3	0.0	0.15
	OTiS-Huge	250	32	1e-3	0.2	0.15

Table 11. Computational resources used to pre-train OTiS. Note that fine-tuning and inference of all OTiS variants on downstream applications were performed using a single NVIDIA RTX A6000-48GB and 32 CPUs.

Model	Parameters	Power consumption	CPU count	GPU		
				Count	Hours	Type
OTiS-Base	8 M	700 W*	128	4	115 <sup>†</sup>	NVIDIA A100-80GB
OTiS-Large	44 M	800 W*	128	4	154 <sup>†</sup>	NVIDIA A100-80GB
OTiS-Huge	131 M	960 W*	128	4	219 <sup>†</sup>	NVIDIA A100-80GB

\* Total power consumption across all GPUs.

<sup>†</sup> Total hours across all GPUs.

regression

$$\mathbf{Y} = \mathbf{1}\beta_0 + \mathbf{X}\mathbf{B} + \boldsymbol{\epsilon} \in \mathbb{R}^{N \times 3} \quad \text{with} \quad \beta_0 \in \mathbb{R}^{1 \times 3}, \mathbf{X} \in \mathbb{R}^{N \times 3}, \mathbf{B} \in \mathbb{R}^{3 \times 3}, \boldsymbol{\epsilon} \in \mathbb{R}^{N \times 3}, \quad (8)$$

where  $\mathbf{1} \in \mathbb{R}^{N \times 1}$  is a vector of ones and  $N$  denotes the number of electrodes, to align the first three principal components in  $\mathbb{E}_X^3$  (here,  $\mathbf{X}$ ) with the 3D electrode coordinates in  $\mathbb{E}_Y^3$  (here,  $\mathbf{Y}$ ). Finally, to quantify this very alignment, we determine the coefficient of determination  $R^2 \in [0, 1]$ . Note that  $R^2 = 1$  represents a perfect alignment, i.e.  $\mathbb{E}_Y^3 = \mathbb{E}_X^3$ , where the first three principal components of the EEG-specific variate embeddings only need to be shifted and scaled to recover the spatial arrangement of the electrodes (i.e.  $\boldsymbol{\epsilon}$  is a zero matrix).

We analyse (i) variate embeddings of 10-20 system EEG recordings with 19 electrodes learned during pre-training and (ii) variate embeddings of previously unseen 10-20 system EEG recordings with 32 electrodes learned during fine-tuning. We find that the first three principal components explain 74.7% of the variance in (i) and 87.9% in (ii). Moreover, we observe  $R^2$  values of 0.81 for (i) and 0.95 for (ii), indicating an accurate alignment of EEG-specific variate embeddings with the electrode layout. A 2D visualisation of this alignment is provided in Figure 8. Overall, these findings confirm our initial hypothesis that the spatial arrangement of EEG electrodes can be precisely recovered from EEG-specific variate embeddings.

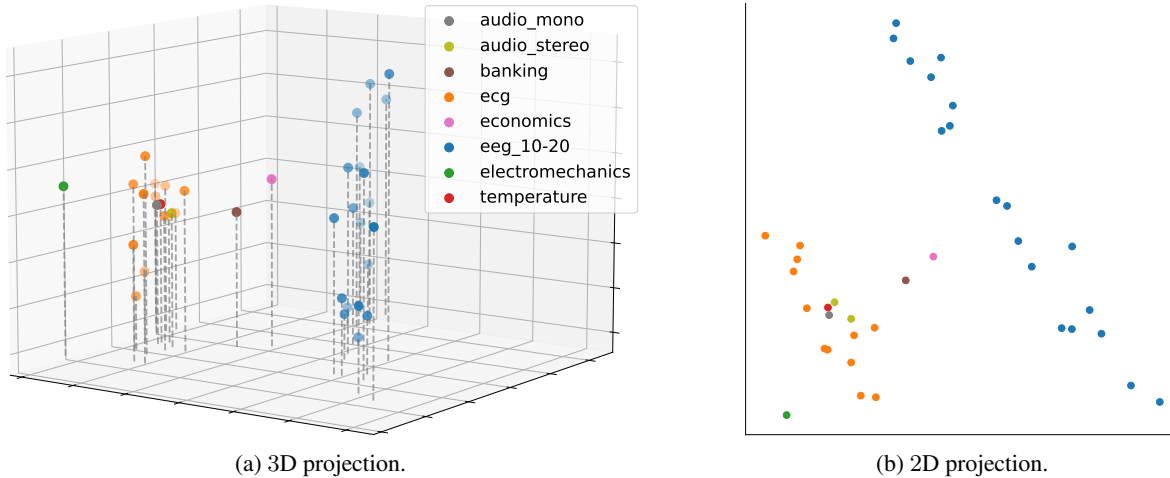


Figure 6. PCA projections of the domain-specific variate embeddings learned during pre-training.  $\text{OTIS}$  unifies time series from diverse domains in a meaningful latent space, while correctly encoding the inter-variate relationships within a domain. Mono ( $\bullet$ ) and stereo ( $\circ$ ) audio-specific embeddings cluster closely together, as do those for banking ( $\bullet$ ) and economics ( $\circ$ ). Clear separation is observed for EEG-specific embeddings ( $\bullet$ ), while also ECG-specific embeddings ( $\circ$ ) form a tight cluster.

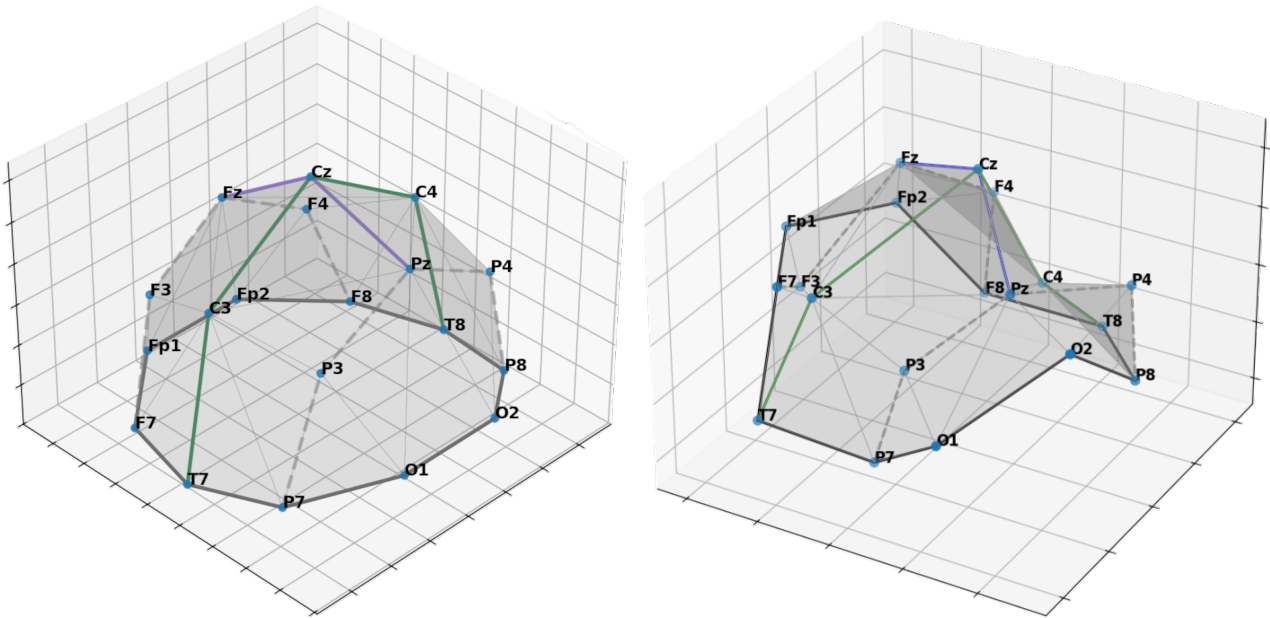
**ECG-Specific Variate Embeddings.** Another application in medicine is electrocardiography (ECG), which is widely used to measure the electrical activity of the heart via electrodes placed on the human torso. The standard 12-lead ECG is composed of 3 limb leads (leads I, II, and III), 3 augmented limb leads (leads aVR, aVL, and aVF), and 6 precordial leads (leads V1 to V6). The limb leads (or Einthoven leads [Einthoven et al. \(1902\)](#)) reflect the *potential differences* between pairs of electrodes attached to the limbs (right arm: RA, left arm: LA, and left leg: LL): I, II, and III represent the potential difference between RA and LA, RA and LL, and LA and LL, respectively. Together, these limb leads form the so called Einthoven triangle [Kligfield et al. \(2007\)](#), spanned by the three vectors  $RA \rightarrow LA$ ,  $RA \rightarrow LL$ , and  $LA \rightarrow LL$ . Similarly, the augmented limb leads (or Goldberger leads [Goldberger \(1942\)](#)) also reflect *potential differences* between pairs of electrodes attached to the limbs. In contrast to the previous leads, however, the precordial leads (or Wilson leads [Wilson et al. \(1934\)](#)) are *directly measured* from the electrodes placed on the chest.

When analysing the latent space of the ECG-specific variate embeddings learned during pre-training, we can clearly observe these relationships among the 12 leads, as depicted in Figure 9. For instance, the limb leads I, II, and III form a planar 2D triangle, thus successfully reflecting Einthoven’s triangle [Kligfield et al. \(2007\)](#). Additionally, the precordial leads V1 to V6, arranged on the rib cage from the sternum to the mid-axillary line, represent the 3D view of the human heart.

**Weather-Specific Variate Embeddings.** We focus the following analysis on the Weather-specific variate embeddings learned during fine-tuning. The central question is whether  $\text{OTIS}$  can learn domain-specific knowledge - in this case, for the weather domain - from limited data seen only during fine-tuning. To investigate this, we compute the cosine similarity for all pairs of Weather-specific variate embeddings, as summarised in Figure 10. Note that these embeddings were randomly initialised and learned specifically for the Weather 2024 dataset during the forecasting task described in Section B. The Weather variates span diverse climatological categories, including temperature (T, Tpot, Tdew, Tlog), humidity (rh, VPmax, VPact, VPdef, sh, H2OC), wind (wv, max. wv, wd), radiation (SWDR, PAR, max. PAR), pressure (p, rho), and precipitation (rain, raining). Our analysis demonstrates that  $\text{OTIS}$  effectively captures complex relationships among these distinct climatological indicators, as detailed in the following discussion.

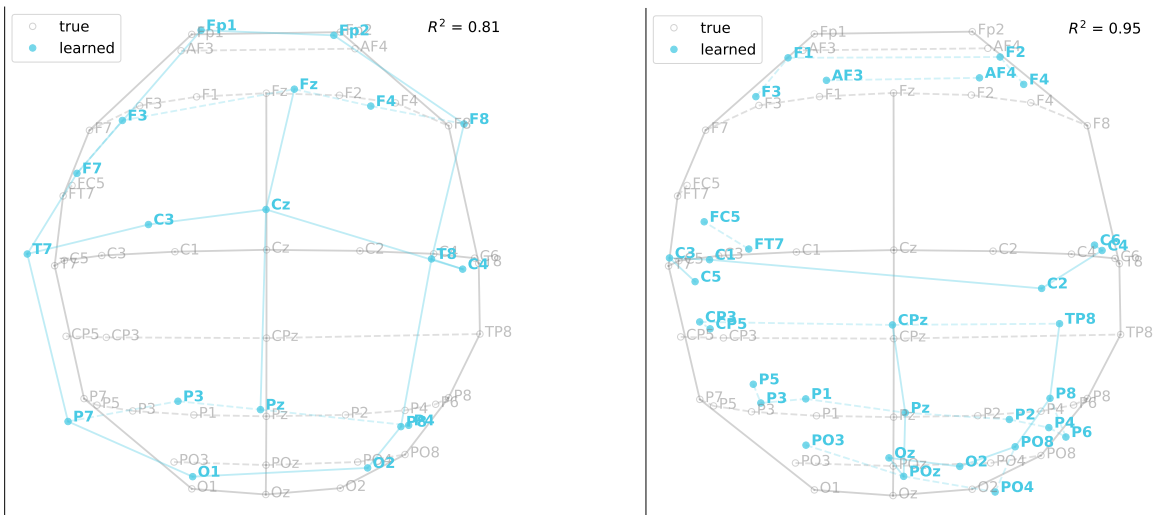
High **positive similarities** typically indicate relationships within a single climatological category. For example, we observe strong similarities among temperature variates, humidity variates, radiation variates, pressure variates, and precipitation variates. These results are expected, as these variates all describe different aspects of the same category and often fluctuate together. Additionally, subtle variations in the similarity scores reveal how, for instance, dew point temperature (Tdew) depends not only on temperature but also on other factors, such as humidity (rh).

High **negative similarities** typically represent relationships across climatological categories. For example, consider the



(a) 3D spatial arrangement of EEG electrodes defined by the international 10-20 system for EEG recordings. (b) First three principal components of EEG-specific variate embeddings.

Figure 7. Analysis of the variate embeddings for 10-20 system EEG recordings with 19 electrodes learned during pre-training. The label of each coordinate corresponds to the electrode name.



(a) Variate embeddings of 10-20 system EEG recordings with 19 electrodes learned during pre-training. (b) Variate embeddings of previously unseen 10-20 system EEG recordings with 32 electrodes learned during fine-tuning.

Figure 8. First two principal components of EEG-specific variate embeddings, overlaid on the true EEG electrode layout. The embeddings accurately reflect the spatial arrangement of the EEG electrodes, confirmed by high correlations ( $R^2$ ) between the principal components ● and the electrode arrangement ○.

inverse relationship between vapor pressure deficit (VPdef) and relative humidity (rh), defined as:

$$VPdef = SVP \left( 1 - \frac{rh}{100} \right), \quad (9)$$

where SVP [mBar] denotes the saturation vapor pressure. Our analysis showcases that OTiS correctly captures this negative correlation, as well as other relationships across categories. These include the inverse correlation between strong winds

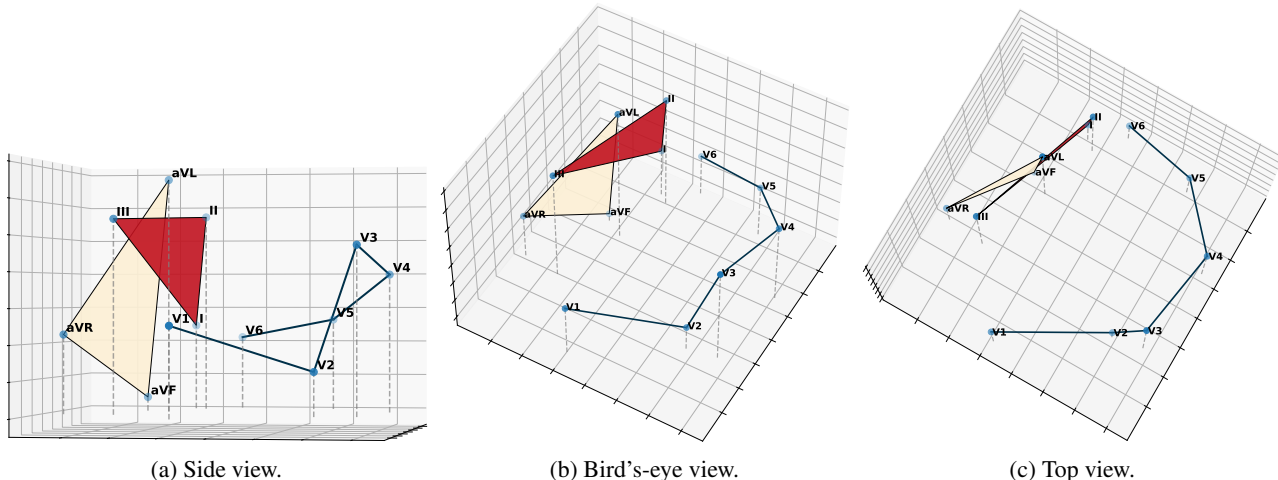


Figure 9. Principal component analysis of the variate embeddings for standard 12-lead ECG learned during pre-training. Their first three components, shown in (a), (b), and (c), accurately reflect the true physiological structure of ECG leads. The V1-V6 leads, arranged on the rib cage from the sternum to the mid-axillary line, represent a 3D view of the human heart. The I-II-III leads and aVR-aVL-aVF leads, derived from electrodes placed on one foot and both arms, form a planar 2D triangle.

(max.  $wv$ ) and low air pressure ( $p$ ), and between extended precipitation (raining) and lower incoming radiation (SWDR).

### E.2.2. TEMPORAL PATTERNS

The central question is whether  $\text{OTiS}$  learns only the correlations across variates or also captures temporal patterns within a variate. To investigate this, we conduct forecasting experiments on uni-variate sine waves with distinct frequencies ranging from 2 Hz to 100 Hz. In this uni-variate setting, we ensure that our model does not leverage information from other variates. For these experiments,  $\text{OTiS}$  remains frozen after pre-training, with only the randomly initialised domain-specific variate embedding (a single embedding for uni-variate data, totalling less than 0.2 k trainable parameters) being fine-tuned on 50 Hz sine waves. During inference, we forecast unseen sine waves with frequencies of 2 Hz, 28 Hz, 60 Hz, and 100 Hz, using the domain-specific variate embedding learned on 50 Hz sine waves. As depicted in Figure 11, the experiments reveal that  $\text{OTiS}$  captures not only inter-variate relationships, but also temporal patterns that generalise to unseen time series.

## F. Zero-Shot Capabilities

To analyse the quality of the time series features extracted by  $\text{OTiS}$ , we conduct zero-shot classification experiments using the Epilepsy 2001, FD-B 2016, Gesture 2009, and EMG 2000 datasets. These datasets ensure high versatility in our analysis, as they differ notably in the number of variates, time points, sampling frequency, as well as number of classes, and cover distinct domains and applications. For these zero-shot experiments,  $\text{OTiS}$  is evaluated directly after pre-training without any fine-tuning, utilising randomly initialised variate embeddings. As no classification head is employed, the encoder’s output tokens are averaged to obtain a global representation for each sample. To generate class logits, pairwise cosine similarity is computed between the global representation of a test sample and each class representation, i.e. the mean of all global representations of the training samples from that class. The class with the highest logit is assigned to the test sample.

As illustrated in Figure 12, our analysis demonstrates that  $\text{OTiS}$  extracts distinct representations for different classes, even without domain-specific fine-tuning. This capability translates to zero-shot classification accuracies of 93.70 % for Epilepsy, 57.87 % for FD-B, 51.67 % for Gesture, and 95.12 % for EMG. Comparing these results with those from fine-tuning in Figure 13, we observe only slight performance decreases for Epilepsy ( $-0.55\%$ ) and EMG ( $-2.44\%$ ), but more substantial gaps for FD-B ( $-41.37\%$ ) and Gesture ( $-11.94\%$ ). A closer comparison of the latent space for FD-B between the zero-shot setup (Figure 12b) and the fine-tuning setup (Figure 13b) reveals that the performance gap arises due to a partial overlap of inputs from classes 1 and 2 in the zero-shot setup. Similarly, the zero-shot latent space shows poor clustering for the eight classes in Gesture (Figure 12c), with notable improvements for classes 0 and 7 after fine-tuning (Figure 13c).

Furthermore, since our pre-training corpus includes EEG (TDBrain 2022 and SEED 2015) and Electromechanics (FD-A

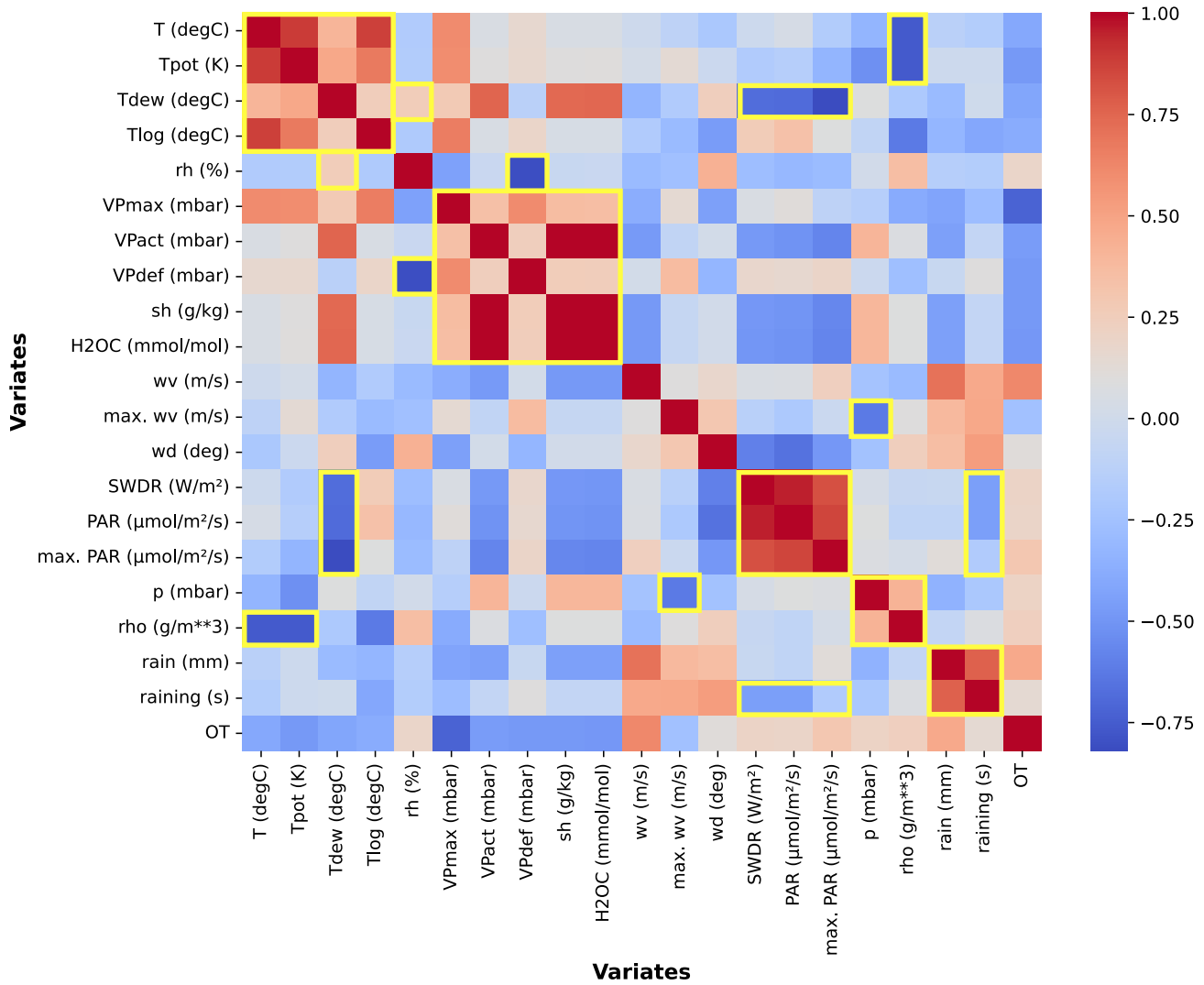


Figure 10. Cosine similarity matrix of Weather-specific variate embeddings. The ordering of the variates was modified for visualisation purposes. Areas with high positive and high negative similarity are exemplary framed in yellow. OTiS successfully learns the non-linear relationships between climatological indicators of the Weather 2024 dataset.

2016) data, we investigate whether performance gains can be achieved by using domain-specific variate embeddings, learned during pre-training, instead of randomly initialised ones. As expected, leveraging these domain-specific embeddings improve the quality of the extracted time series features, resulting in zero-shot classification accuracies of 95.18% for Epilepsy (+1.48%) and 61.32% for FD-B (+3.45%). Interestingly, the improved zero-shot performance for Epilepsy even surpasses that of fine-tuning. Overall, these zero-shot experiments indicate a high quality of the readily available time series features extracted by OTiS, which can be further refined through domain-specific knowledge, including domain-specific variate embeddings or fine-tuning.

## G. Additional Ablation Studies

### G.1. Dual Masking Strategy

To enhance OTiS' foundational capabilities for general time series analysis, we utilise a dual masking strategy during pre-training, as described in Section 3.4. Specifically, we alternate between two masking schemes during pre-training: random masking (randomly masking across variate and temporal dimension) and post-fix masking (masking the second half of the temporal dimension). To determine the optimal balance between these two schemes, we evaluate different

## Fine-tuning on 50Hz sine waves (&lt; 0.2k trainable parameters)

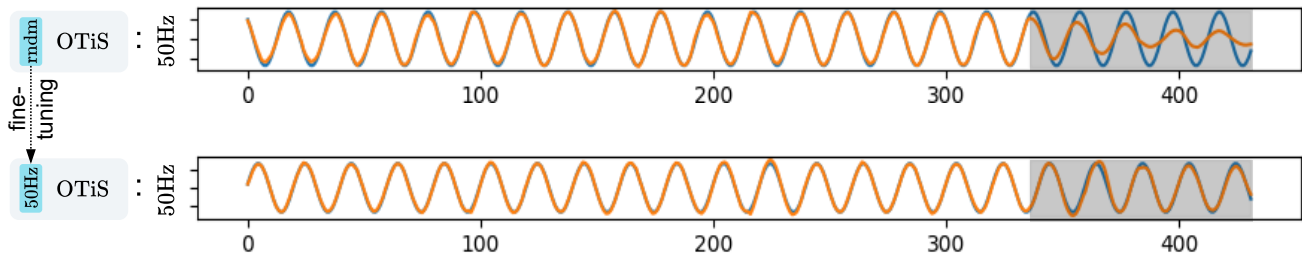
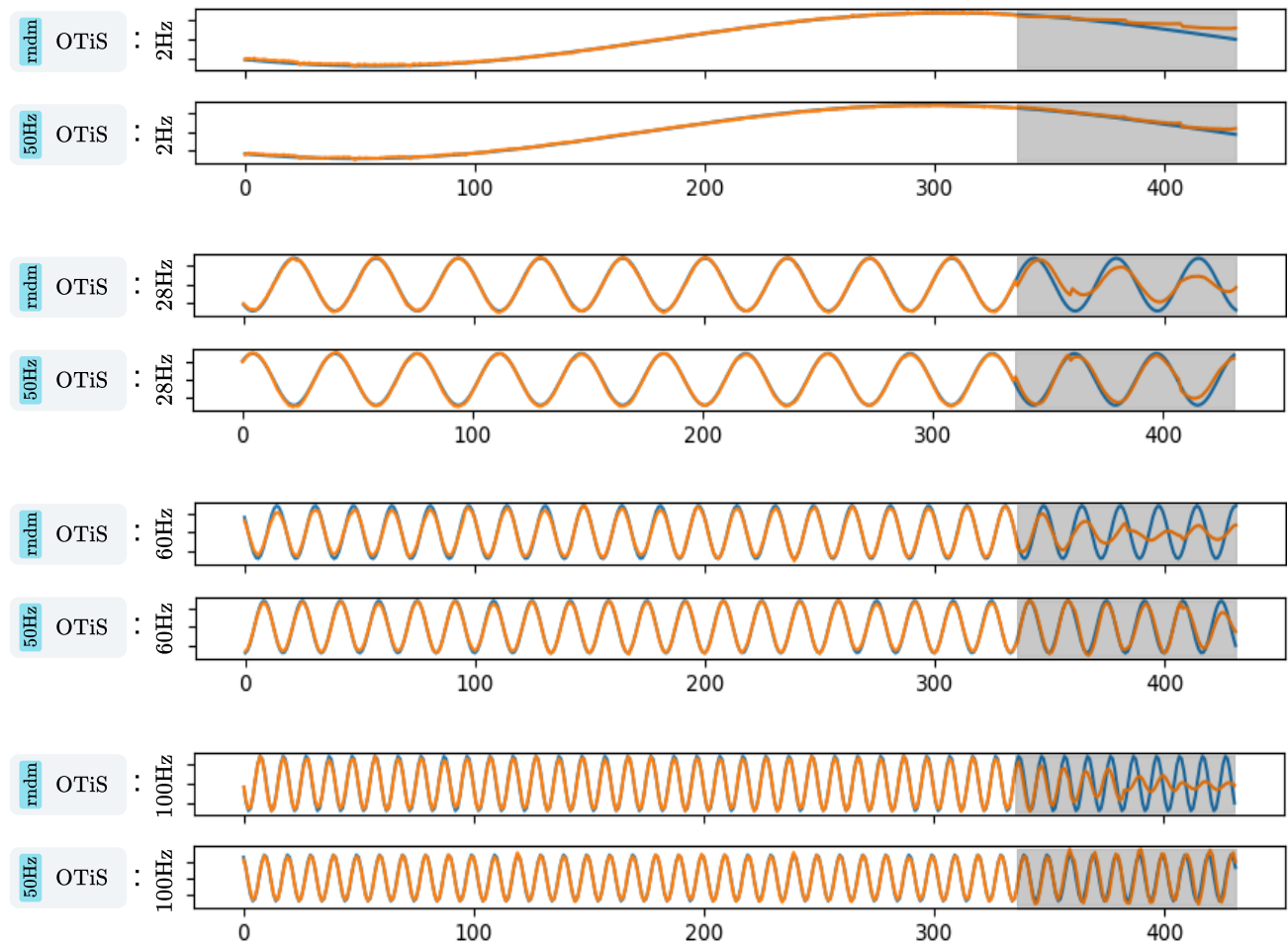
Inference on *unseen* sine waves (0 trainable parameters)

Figure 11. Visualisation of OTiS-Base forecast predictions on sine waves. A forecasting horizon of 96 time points is predicted from the past 336 time points. Ground truth in blue, prediction in orange. Areas highlighted in grey are not visible to the model. During fine-tuning, OTiS remains frozen after pre-training, with only the randomly initialised domain-specific variate embedding (< 0.2k parameters) being trained. During inference, OTiS is fully frozen and forecasts are made on *unseen* sine waves. The domain-specific variate embedding trained on 50 Hz sine waves effectively captures temporal patterns that generalise to sine waves of previously unseen frequencies.

compositions of the dual masking strategy across the general use cases in time series analysis. Our analysis reveals that a combination of 75 % random masking and 25 % post-fix masking consistently yields the best downstream performance

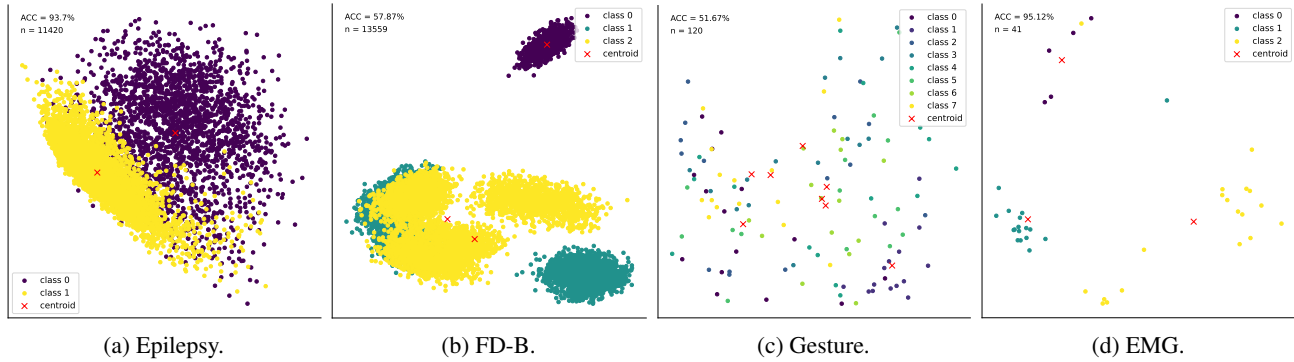


Figure 12. First two principal components of *zero-shot* representations generated by OTiS-Base. In this setup, OTiS is evaluated after pre-training without any fine-tuning, utilising randomly initialised variate embeddings. As no classification head is employed, the output tokens of the encoder are averaged to obtain a global representation. OTiS generates distinct representations for different inputs, even across domains and tasks, highlighting the quality of its extracted time series features.

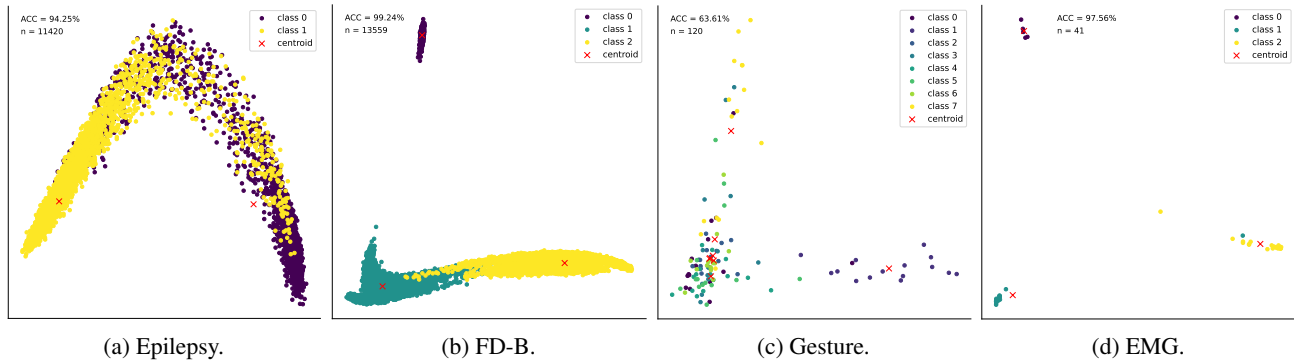


Figure 13. First two principal components of *fine-tuned* representations generated by OTiS-Base. In this setup, OTiS is fully fine-tuned, along with a classification head, after pre-training. To enable a fair comparison, the global representations obtained by averaging the encoder’s output tokens are visualised. Incorporating domain-specific knowledge through fine-tuning enables OTiS to effectively tailor its feature extraction to the specific domain and task.

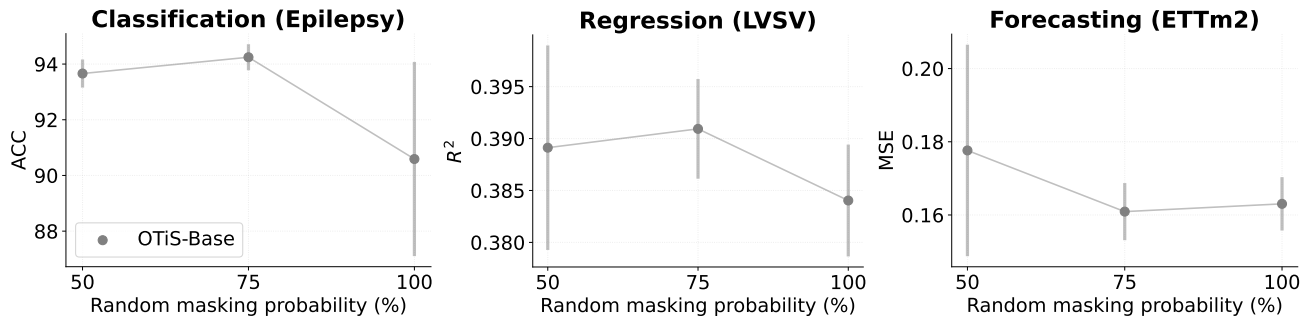


Figure 14. Ablation study on the composition of the dual masking strategy. Error bars represent the standard deviation across 5 seeds. A combination of 75 % random masking and 25 % post-fix masking during pre-training consistently yields the best downstream performance across tasks.

across all tasks, as illustrated in Figure 14.

## G.2. Pre-Training Strategy

To explore whether domain-specific pre-training offers advantages over pre-training on diverse time series across domains, we analyse various training strategies for EEG event type classification using the TUEV 2016 dataset, as summarised in Table 12. In particular, we evaluate three different training strategies for our model: fully supervised training from scratch ( $\text{OTiS-Base}_{\text{w/o pre-training}}$ ), pre-training exclusively on EEG datasets ( $\text{OTiS-Base}_{\text{EEG}}$ ), and pre-training across domains ( $\text{OTiS-Base}$ ). Additionally, we analyse whether domain-specific variate embeddings learned during pre-training are required for competitive downstream performance, or if randomly initialised variate embeddings (rVE) are sufficient. We compare  $\text{OTiS}$  against both task-specific and foundation models that are particularly designed for EEG analysis. The task-specific models (either fully supervised or pre-trained and fine-tuned on the target dataset) include ST-Transformer (Song et al., 2021), CNN-Transformer (Peh et al., 2022), FFCL (Li et al., 2022), SPARCNet (Jing et al., 2023), and ContraWR (Yang et al., 2023). The foundation models (pre-trained on a large medical time series corpus and fine-tuned on the target dataset) include BIOT (Yang et al., 2024) and LaBraM (Jiang et al., 2024). Further details on training strategies and architectural design are provided in Table 5 of Section B.

The experiments show that pre-trained models consistently outperform fully supervised models trained from scratch. However, our fully supervised model,  $\text{OTiS-Base}_{\text{w/o pre-training}}$ , is superior to task-specific models and performs on par with the foundational BIOT model, indicating an efficient interplay between the domain-specific tokeniser and the encoder. We also observe that competitive performance can be achieved even without explicit domain knowledge, as indicated by the results of  $\text{OTiS-Base}_{\text{EEG w/rVE}}$ . Interestingly, we find that pre-training  $\text{OTiS}$  exclusively on EEG data does not yield better results compared to pre-training across diverse domains. These observations emphasise that expanding the pre-training corpus with time series from diverse domains enhances the overall quality of extracted time series features, which is especially beneficial when domain-specific data is scarce. Optimal performance within a specific domain requires pre-training on large, domain-specific corpora, which provide comprehensive domain knowledge and translate into superior downstream results, as evidenced by the performance of LaBraM. However, this approach is often hindered by the limited availability of domain-specific data, particularly in medical applications. In such cases, our approach offers a promising solution to address data scarcity by leveraging readily available data from other domains.

## H. Forecast Visualisation

We visualise the performance of our model on 6 forecasting benchmarks in Figure 15.



Table 12. Ablation study on training strategies for EEG event type classification on TUEV 2016. Mean and standard deviation is reported across 5 seeds. Best score in **bold**, second best underlined. Note that PT refers to pre-trained models. Expanding the EEG pre-training corpus of OTiS with time series from other domains improves the overall quality of the extracted EEG features.

Methods	PT	Params	Balanced ACC $\uparrow$	Cohen’s Kappa $\uparrow$	Weighted F1 $\uparrow$
ST-Transformer 2021	$\times$	3.5 M	$0.3984 \pm 0.0228$	$0.3765 \pm 0.0306$	$0.6823 \pm 0.0190$
CNN-Transformer 2022	$\times$	3.2 M	$0.4087 \pm 0.0161$	$0.3815 \pm 0.0134$	$0.6854 \pm 0.0293$
FFCL 2022	$\times$	2.4 M	$0.3979 \pm 0.0104$	$0.3732 \pm 0.0188$	$0.6783 \pm 0.0120$
SPaRCNet 2023	$\times$	0.8 M	$0.4161 \pm 0.0262$	$0.4233 \pm 0.0181$	$0.7024 \pm 0.0104$
ContraWR 2023	$\checkmark$	1.6 M	$0.4384 \pm 0.0349$	$0.3912 \pm 0.0237$	$0.6893 \pm 0.0136$
BIOT <sup>+</sup> 2024	$\checkmark$	3.2 M	$0.5281 \pm 0.0225$	$0.5273 \pm 0.0249$	$0.7492 \pm 0.0082$
LaBraM <sup>□</sup> 2024	$\checkmark$	369 M	<b><math>0.6616 \pm 0.0170</math></b>	<b><math>0.6745 \pm 0.0195</math></b>	<b><math>0.8329 \pm 0.0086</math></b>
OTiS-Base <sub>w/o</sub> pre-training <sup>*</sup>	$\times$	8 M	$0.5361 \pm 0.0350$	$0.5183 \pm 0.0316$	$0.7642 \pm 0.0157$
OTiS-Base <sub>EEG</sub> <sup>†</sup>	$\checkmark$	8 M	$0.5562 \pm 0.0106$	$0.5504 \pm 0.0204$	$0.7784 \pm 0.0095$
OTiS-Base <sub>EEG w/ rVE</sub> <sup>†▷</sup>	$\checkmark$	8 M	$0.5413 \pm 0.0302$	$0.5631 \pm 0.0299$	$0.7860 \pm 0.0120$
OTiS-Base	$\checkmark$	8 M	<u><math>0.5743 \pm 0.0257</math></u>	<u><math>0.5913 \pm 0.0146</math></u>	<u><math>0.8004 \pm 0.0071</math></u>
OTiS-Base <sub>w/ rVE</sub> <sup>▷</sup>	$\checkmark$	8 M	<u><math>0.5728 \pm 0.0134</math></u>	<u><math>0.5772 \pm 0.0281</math></u>	<u><math>0.7922 \pm 0.0127</math></u>

<sup>+</sup> Model was pre-trained on 6 EEG datasets, including TUEV 2016, with more than 13, 000 recording hours.

<sup>□</sup> Model was pre-trained on 16 EEG datasets, including data from the TUH EEG corpus 2016, with more than 2, 500 recording hours.

<sup>\*</sup> Model was randomly initialised and trained fully supervised.

<sup>†</sup> Model was pre-trained on EEG datasets of our pre-training corpus, i.e. TDBrain 2022 and SEED 2015, totalling 125 recording hours.

<sup>▷</sup> Variate embeddings (VE) are randomly (r) initialised before for fine-tuning.

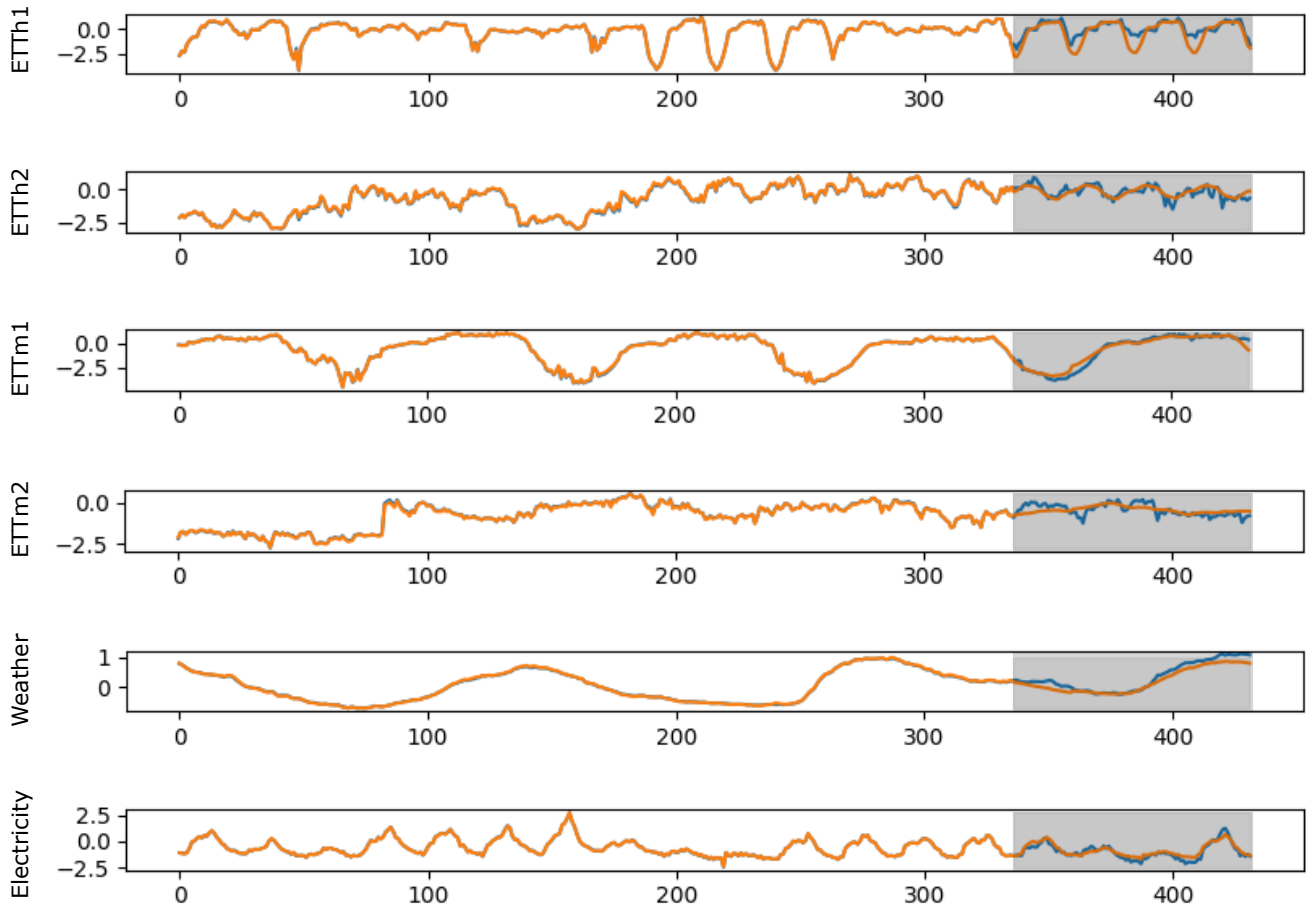


Figure 15. Visualisation of  $\text{OTIS-Base}$  forecast predictions on 6 benchmark datasets. A forecasting horizon of 96 time points is predicted from the past 336 time points. Ground truth in blue, prediction in orange. Areas highlighted in grey are not visible to the model.